Title:

Structure and assembly of Borna disease virus 1 nucleoprotein–RNA complexes

Authors

Yukihiko Sugita (杉田征彦)[1,2,3,*,†], Yuya Hirai (平井悠哉)[4,*,†], Shinya H. Goto (後藤真也)[2,3], Keizo Tomonaga (朝長啓造)[5,6,7], Takeshi Noda (野田岳志)[2,3,8], Masayuki Horie (堀江真行)[1,5,9,10,†]

Affiliations

[1] Hakubi Center for Advanced Research, Kyoto University, Kyoto, Kyoto, 606-8507, Japan

[2] Laboratory of Ultrastructural Virology, Department of Virus Research, Institute for Life and Medical Sciences, Kyoto University, Kyoto, Kyoto, 606-8507, Japan

[3] Graduate School of Biostudies, Kyoto University, Kyoto, Kyoto, 606-8507, Japan

[4] Department of Biology, Osaka Dental University, Hirakata, Osaka, 573-1121, Japan

[5] Laboratory of RNA Viruses, Department of Virus Research, Institute for Life and Medical Sciences, Kyoto University, Kyoto, Kyoto, 606-8507, Japan

[6] Laboratory of RNA Viruses, Department of Mammalian Regulatory Network, Graduate School of Biostudies, Kyoto University, Kyoto, Kyoto, 606-8507, Japan

[7] Department of Molecular Virology, Graduate School of Medicine, Kyoto University, Kyoto, Kyoto, 606-8507, Japan

[8] Institute for Integrated Cell-Material Sciences, Kyoto University, Kyoto, Kyoto, 606-8501, Japan

[9] Laboratory of Veterinary Microbiology, Graduate School of Veterinary Science, Osaka Metropolitan University, Izumisano, Osaka, 598-8531, Japan

[10] Osaka International Research Center for Infectious Diseases, Osaka Metropolitan University, Osaka, 545-0051, Japan

[*] These authors contributed equally to this work.

[†] Corresponding authors: sugita.yukihiko.8w@kyoto-u.ac.jp (YS), hirai-y@cc.osaka-dent.ac.jp (YH), mhorie@omu.ac.jp (MH)

Keywords

Borna disease virus 1; mononegavirus; negative-strand RNA virus; nucleoprotein; nucleocapsid; cryo-EM

Abstract

Structures of nucleoprotein (N)–RNA complexes of the *Bornaviridae*, a virus family in the order *Mononegavirales*, have remained unknown. Using cryo-electron microscopy (cryo-EM), we characterized N structures of Borna disease virus 1 (BoDV-1), the type species of the *Bornaviridae,* which causes fatal human encephalitis. N forms complexes in both RNA-free and RNA-bound states, revealing conserved features throughout the order, as well as BoDV-1-specific stoichiometry, thereby offering insights into viral evolution. We redefine assembly principles governing N–RNA complexes with the discovery of a previously unrecognized, RNA-independent mechanism involving domain-swapping and truncated subunits. Mutational analyses identified residues essential for nucleocapsid formation and RNA synthesis. Cryo-EM of mutant complexes captured RNA-free assemblies, suggesting that initial N oligomerization precedes RNA binding. These findings explain several unknowns in N–RNA complex structure and suggest an alternative to canonical RNA-driven assembly models, offering a new conceptual framework for nucleocapsid formation.

Introduction

Viruses classified in the order *Mononegavirales* typically possess a linear, non-segmented, negative-strand, single-stranded RNA genome. They infect a wide range of host species in the kingdoms *Animalia*, *Plantae*, and *Fungi*[1]. Mononegaviruses infecting humans are classified into five families: *Filoviridae* (Ebola and Marburg viruses [EBOV, MARV]), *Paramyxoviridae* (measles and Nipah viruses [MV, NiV]), *Rhabdoviridae* (rabies virus [RABV]), *Pneumoviridae* (human respiratory syncytial virus [HRSV]), and *Bornaviridae*, represented by BoDV-1. RNA genomes of these viruses are encapsidated by multiple copies of the viral N molecule that form N–RNA complexes. N–RNA complexes are scaffolds for binding to the viral phosphoprotein (P) and RNA-dependent RNA polymerase (L), and for assembling into functional viral nucleocapsids responsible for viral RNA transcription and replication. In infected cells, biomolecular condensates known as viral inclusion bodies (IBs) are formed as membraneless compartments in which nucleocapsid assembly and viral RNA synthesis are spatially coordinated[2–5].

Given the essential roles of nucleocapsid architecture in viral replication, extensive structural studies have been conducted on mononegavirus N molecules. A previous X-ray crystallography study provided the first high-resolution structure of a negative-strand RNA virus N by resolving BoDV-1 N in an RNA-free, planar tetrameric complex[6]. This structure exhibited a unique bilobed α-helical fold, composed of N-terminal and C-terminal lobes connected by a linker and flanked by extended N- and C-terminal arm domains (Supplementary Fig. 1A). Structural studies of other mononegavirus families have confirmed the conservation of this bilobed core and extended-arm motif[7–17], with RNA-binding consistently occurring in a “cleft” between the lobes, as revealed by multiple N–RNA complex structures[7, 8, 10, 11, 16, 18]. Furthermore, cryo-EM studies of various species have demonstrated structural conservation, particularly at the individual protein level in the same virus families[19–22], and revealed diverse, oligomeric arrangements of N complexes in both RNA-bound and RNA-free states[23–25].

BoDV-1, the type species of the family *Bornaviridae*, is a neurotropic pathogen of considerable public health concern, causing fatal encephalitis in various mammals, including humans[26]. Unlike other human mononegaviruses that replicate in the cytoplasm, BoDV-1 replicates in the nucleus of host cells, where the nucleocapsid associates with host chromatin, facilitating persistent infection through successive host cell divisions[27]. Given its public health relevance and a unique viral life cycle, structural characterization of BoDV-1 N is particularly important. Discovering structural variability, even in RNA-free states, provides critical insights into N complex dynamics, which are essential for understanding nucleocapsid assembly, genome encapsidation, and the unique nuclear replication strategy employed by BoDV-1. However, structural knowledge remains limited to a single RNA-free crystal structure for the family *Bornaviridae*[6]. Among the five families in *Mononegavirales* that include human-infecting viruses, *Bornaviridae* is the only one for which the N–RNA complex structure has not been characterized, representing a critical and long-standing gap in our understanding of the structural properties of viral N molecules. This gap has hindered comparative and evolutionary understanding of RNA encapsidation principles among mononegavirus families.

In addition, although previous N–RNA complex structures revealed overall architectures, they offered limited insight into how N oligomerizes and binds RNA during encapsidation. It remains unclear whether RNA is required to initiate the assembly process or whether N can form modular pre-assembled complexes that subsequently engage RNA.

To address this question, we employed single-particle cryo-EM to reveal high-resolution structures of BoDV-1 N complex in diverse RNA-free and RNA-bound oligomeric states. These analyses captured a broad range of assembly states and conformations, including unreported configurations such as N-terminally truncated subunits. Structure-guided mutational studies, including characterization of key residues, such as Lys164, have identified the RNA binding mechanism and the fundamental structural principle required for IB formation and viral RNA synthesis in host cells. These findings offer critical molecular details about unique assembly mechanisms of BoDV-1 N, contributing to our understanding of mononegavirus RNA encapsidation strategies and molecular evolution. Moreover, high-resolution structures obtained here provide a foundation for rational antiviral design targeting critical N–RNA interactions against BoDV-1 and related viruses.

Results

Protein purification and structural analysis of full-length BoDV-1 N complexes

Full-length BoDV-1 N with an N-terminal hexahistidine tag was expressed in *E. coli* and purified using affinity chromatography followed by size-exclusion chromatography (SEC) (Supplementary Fig. 1A-B). Purified N protein eluted predominantly as a single peak during SEC, and the peak fraction exhibited a low 260/280 nm absorbance ratio (0.66), indicating minimal RNA inclusion. Cryo-EM analysis revealed that this fraction predominantly contained planar tetrameric complexes, which closely resembled the RNA-free N tetrameric structure previously reported using X-ray crystallography (Supplementary Fig. 1C, D)[6].

In contrast, an earlier-eluting SEC fraction displayed a higher A260/A280 ratio of 1.36, suggesting the presence of substantial RNA. Cryo-EM analysis revealed structurally diverse N complexes (Supplementary Fig. 1E). Single-particle cryo-EM analysis identified complexes consisting of varying numbers of N subunits, including ring-like, S-shaped, and triangular configurations, ranging from tetramers to larger assemblies of up to thirteen subunits. Distinct densities attributable to RNA were observed in some of these complexes.

In total, we identified sixteen distinct N complex types, of which fifteen were reconstructed to three-dimensional (3D) structures at resolutions ranging from 2.8 to 8.6 Å, excluding the nonameric ring-like structure (Supplementary Fig. 1F-G and Supplementary Table 1). For reconstructions better than 4 Å resolution, atomic models were built based on well-resolved protein backbone, with side-chain densities frequently visible, allowing for detailed interpretation of molecular architecture.

Furthermore, cryo-EM data showed considerable structural heterogeneity, with continuous conformational variability observed in each oligomeric species (Supplementary Movie 1). This heterogeneity suggests that N molecules and their assemblies possess intrinsic dynamic flexibility.

Importantly, similar oligomeric assemblies were observed when N protein was expressed in human cells (Supplementary Fig. 1H). These findings support the notion that such assemblies can form under host cell conditions, underscoring their potential relevance during natural infection.

Overall structures of RNA-free, ring-like N tetramers and pentamers

Crystal structures may differ from solution-state conformations due to crystal packing constraints. To determine whether cryo-EM structures of RNA-free N complexes matched the previously reported crystal structure, we examined their architecture and conformational variability in solution.

Cryo-EM analysis revealed two slightly different conformations of the tetrameric N complex, exhibiting cyclic 4-fold (C4) symmetry (Fig. 1A-B). Both conformations maintained a conserved core architecture, characterized by interactions mediated by N- and C-terminal arm domains between adjacent subunits. The primary structural difference between these two conformations was observed in the relative orientation of the C-terminal domains, which differed by an ~8.5° rotational shift (Supplementary Fig. 2A). Structural alignment demonstrated high similarity between one cryo-EM tetramer conformation (class 1: “4-mer-1”) and the crystal structure at the monomeric level, with a backbone root-mean-square deviation (RMSD) of 0.70 Å. However, the crystal structure appeared slightly more compact, likely due to packing-induced constraints (Supplementary Fig. 2B). This similarity suggests that crystal packing effects alone do not shape the tetrameric arrangement observed in the crystal structure, but reflect an inherently stable configuration adopted by the protein in solution.

The second tetrameric conformation (class 2: “4-mer-2”) exhibited an RMSD of 1.27 Å compared to the 4-mer-1 structure. In 4-mer-2, residue Arg341 at the boundary between adjacent C-terminal lobes adopted a different rotamer conformation, resulting in notable divergence in inter-subunit distances (Fig. 1C, D).

We also identified and reconstructed the 3D structure of an RNA-free ring-like pentameric N complex (“5-mer”) at an overall resolution of 3.8 Å. This structure displays ring-like morphology with pseudo-C5 symmetry (Fig. 1E). Similar to the tetramers, pentameric subunits interact via their N- and C-terminal arms, with high structural conservation observed in the core domain (residues 44-341). Despite this conservation, the 5-mer exhibits intrinsic asymmetry, with subtle positional deviations among subunits (Fig. 1F).

In both tetrameric and pentameric configurations, several regions displayed reduced map density indicative of intrinsic flexibility or disorder (Supplementary Fig. 2A-H). Specifically, residues at approximately positions 1-24 and 316-323 consistently show low local resolution, consistent with previous crystallographic observations. Additionally, the loop in the

165 protruding β strands (residues approximately 106-111) could not be modeled due to
166 insufficient map density.

167 Local resolution of the maps and *B*-factor of the models were also poor for residues 38-42,
168 which form the connecting part of the N-terminal arm and N-terminal lobe, residues 120-127,
169 a relatively long loop region largely exposed to the solution, and residues 347-354
170 surrounding the linker region between the C-terminal lobe and C-terminal arm helix. These
171 findings suggest enhanced local mobility in solution.

172 The low *B*-factor of the N-terminal arm was particularly pronounced in one subunit (N_5) of
173 the pentameric structure, contributing to asymmetry and local heterogeneity (Supplementary
174 Fig. 2E). This structural asymmetry and localized disorder likely reflect transient inter-
175 subunit interactions and inherent plasticity of these oligomeric complexes.

176 Collectively, these observations highlight the dynamic behavior of the N assemblies, which
177 may facilitate transitions required for nucleocapsid assembly.

178 **N-N interactions in tetramers and pentamers**

179 The previously reported crystal structure of the RNA-free tetrameric N complex identifies
180 four distinct N-N interaction clusters crucial for maintaining complex stability. These
181 interaction clusters comprise: (1) hydrophobic and electrostatic interactions between the N-
182 terminal arm of one subunit (N_n) and a shallow groove on the N-terminal lobe of the adjacent
183 subunit (N_{n+1}); (2) polar interactions between the N-terminal lobes of adjacent subunits (N_n
184 and N_{n+1}); (3) polar interactions between the C-terminal lobes of adjacent subunits (N_n and
185 N_{n-1}); and (4) hydrophobic and electrostatic interactions linking the C-terminal arm helix of
186 one subunit (N_n) with the C-terminal lobe of the neighboring subunit (N_{n-1}) (Fig. 1G).

187 To assess modes of N-N interactions in our RNA-free N complexes, we analyzed interfaces
188 in tetrameric and pentameric assemblies (Fig. 1G-I). The 4-mer-1 shows N-N interactions
189 consistent with those observed in the crystal structure, with all four interaction clusters
190 preserved. However, 4-mer-2 displays reduced contacts between adjacent C-terminal lobe
191 interfaces, which results from a rotational shift and torsion in domain orientation (Fig. 1H).

192 In the pentameric complex, interactions mediated by N- and C-terminal arm domains were
193 maintained, as in the tetramers. However, polar contacts between lobe domains are generally
194 reduced and vary notably across subunits, reflecting inherent asymmetry and structural
195 plasticity (Fig. 1I).

196 These cryo-EM observations indicate that the stability of RNA-free N complexes is primarily
197 governed by interactions involving terminal arm domains. More transient polar interactions
198 between lobe domains occur across solvent-exposed, loosely packed interfaces, suggesting a
199 dynamic equilibrium in solution. This behavior parallels observations in ring-like N–RNA
200 complexes of HRSV[10] and inter-strand N-N interactions in EBOV helical
201 nucleocapsids[16].

202 **Structures of ring-like N–RNA complexes and N-RNA interactions**

203 Previous structural studies on mononegavirus N–RNA complexes revealed distinct RNA
204 binding modes: RNA is located externally in complexes in the family *Paramyxoviridae*,
205 *Pneumoviridae*, and *Filoviridae*, but encapsidated internally in *Rhabdoviridae*
206 (Supplementary Fig. 3A-D). Despite these differences in RNA positioning, a conserved
207 feature across mononegaviruses is that RNA binds to a cleft formed between the N- and C-
208 terminal lobes of the N molecule. However, for BoDV-1, precise positioning has remained
209 controversial, with reports suggesting either an external location, opposite the cleft[6], or an
210 internal binding mode in the cleft[28].

211 To clarify the RNA binding mode of BoDV-1, we analyzed BoDV-1 hexameric, heptameric,
212 and octameric N–RNA complexes, termed "6-mer", "7-mer", and "8-mer", respectively.
213 These structures demonstrate conclusively that the RNA strand resides in the ring-like
214 complexes and binds to the inter-lobe cleft, a mode previously observed only in
215 *Rhabdoviridae* (Fig. 2A-D, S3D, E). The BoDV-1 N–RNA complex features a gear-like
216 round structure with abrupt changes in RNA backbone curvature, also similar to
217 rhabdoviruses, but distinct from other mononegaviruses (Fig. 2E and S3A-E).

218 Notably, BoDV-1 N exhibits unique RNA-binding stoichiometry, with each N subunit
219 binding eight nucleotides arranged in a sharply bending '4-bases-inside, 4-bases-outside'
220 configuration. This mode is unprecedented in the order *Mononegavirales* (Fig. 2F-G).

221 Consistent with other mononegaviruses, RNA binding in BoDV-1 N is predominantly
222 electrostatic, mediated by interactions between basic amino acid residues and RNA phosphate
223 groups (Fig. 2F). Sequence alignment in the genus *Orthobornavirus* shows that these
224 residues, including Lys154, Lys164, Arg165, Arg297, and Arg321, are highly conserved
225 (Supplementary Fig. 3F). These conserved interactions indicate that N primarily recognizes
226 RNA via its phosphate backbone and local conformation (Fig. 2G). This backbone-dependent
227 RNA recognition provides a mechanistic explanation for the previously reported sequence
228 preference in BoDV-1 N–RNA interactions. The apparent specificity likely arises from
229 structural complementarity between the RNA backbone and the binding cleft of N, rather
230 than from direct base-specific contacts[28].

231 **Local conformational transition of N upon RNA binding**

232 Mononegavirus N molecules cooperatively transition from monomeric RNA-free states to
233 oligomeric RNA-bound states during virus assembly (Supplementary Fig. 3G-J, L-O).
234 Therefore, it is crucial to examine how N molecules undergo conformational changes upon
235 RNA binding to identify the mechanism of nucleocapsid assembly.

236 To explore structural differences upon RNA encapsidation, we compared RNA-free and
237 RNA-bound BoDV-1 N complex structures, 4-mer-2 and 6-mer. The overall structure and
238 relative orientation of N- and C-terminal lobe domains (residues 44-341) remain consistent
239 between RNA-free and RNA-bound states, similar to observations in rhabdoviruses
240 (Supplementary Fig. 3J, O), excluding a hinge-like conformational change observed in
241 paramyxoviruses and pneumoviruses (Fig. 2H, S3G, H, L, M). Regions of poor local
242 resolution, indicative of high local flexibility, are also similar between the two states
243 (Supplementary Fig. 2D-G, S2I-J). However, a local structural transition was observed in the
244 loop region (residues 314-322) of the C-terminal lobe. This region, disordered in RNA-free
245 complexes, becomes ordered and adopts a short helix with a 3_{10} geometry upon RNA binding
246 (Fig. 2I). This loop-to-helix transition resembles that observed in filoviruses[29, 20],
247 suggesting a conserved RNA-binding mechanism across the *Mononegavirales*
248 (Supplementary Fig. 3I, K, N, P). The high-resolution cryo-EM map allowed unambiguous
249 modeling of this helix, confirming the loop-to-helix transition as a definitive structural
250 feature induced by RNA binding. Although this region does not consistently adopt a defined
251 secondary structure formation in other mononegaviruses, its recurrent alignment parallel to
252 the RNA supports its designation as the "RNA-binding loop", a structurally and functionally
253 conserved feature across the order (Supplementary Fig. 3Q-U).

254 In BoDV-1 N–RNA complexes, inter-subunit interactions primarily involve extended N- and
255 C-terminal arm domains (Fig. 2D), with variations in angles and distances between subunits,
256 analogous to RNA-free tetrameric and pentameric complexes (Fig. 2H). Compared to RNA-
257 free tetramers, RNA-bound hexamer displays a wider ring architecture due to the outward

258 swing of the arm domains upon RNA binding (Fig. 2H, bottom). This outward movement
259 creates larger inter-subunit gaps and reduces the contact surface area between the core
260 domains (Fig. 1G-I and 2J). This is accompanied by a flipping-in of Arg341 side chain at the
261 inter-subunit interface, as also observed in 4-mer-2 complex (Fig. 1D, 2H, K).

262 Collectively, these findings indicate that the conformational transition of BoDV-1 N upon
263 RNA encapsidation primarily involves local restructuring of the RNA-binding loop, while the
264 overall oligomeric architecture remains largely preserved. The more open ring-like
265 architecture observed in RNA-bound assemblies, characterized by increased inter-subunit
266 spacing and a broadened internal channel, appears to reflect intrinsic conformational
267 flexibility of N that enables RNA accommodation.

268

269 **Conformational plasticity and RNA binding heterogeneity in hexameric N complexes**

270 In addition to hexameric complexes displaying distinct RNA densities, we identified
271 structurally variable hexameric ring-like assemblies that exhibit variable degrees of
272 circularity (Fig. 3A-C). The most elongated form, hereafter referred to as the "Flat 6-mer",
273 shows no detectable RNA density in the RNA-binding cleft, indicating that it represents an
274 RNA-free state (Fig. 3A, D). A second, more oval-shaped assembly ("Oval 6-mer-1")
275 contains additional density at its center that is not attributable to RNA, potentially
276 corresponding to a folded polypeptide or proteinaceous component. Due to limited local
277 resolution, the identity of this component remains unclear. This complex also lacks visible
278 RNA in the canonical RNA-binding cleft (Fig. 3B, E). A third assembly, "Oval 6-mer-2",
279 exhibits weak, but discernible RNA density in the cleft, suggesting the possibility of partial
280 RNA occupancy or transient interactions (Fig. 3C, F). These structural variations collectively
281 demonstrate that hexameric N complexes can adopt similar global architectures regardless of
282 their RNA-bound state.

283 Cryo-EM density corresponding to the RNA-binding loop varied among the three hexamers.
284 In the RNA-free Flat 6-mer, this region appears poorly resolved, consistent with increased
285 conformational flexibility or disorder, as also observed in RNA-free tetramers and pentamers
286 (Fig. 3D). In contrast, the Oval 6-mer-1 shows density indicative of a helical secondary
287 structure, although some adjacent loop regions remain less well defined (Fig. 3E). The RNA-
288 bound Oval 6-mer-2 exhibits a well-ordered helical conformation similar to that in both Oval
289 6-mer-1 and the fully RNA-bound 6-mer complex (Fig. 3F, G).

290 These findings suggest that the helical conformation in the RNA-binding loop region is not
291 pre-formed, but is instead induced upon interaction with either an RNA molecule, as in Oval
292 6-mer-2, or possibly a proteinaceous component, as suggested in Oval 6-mer-1.

293 **Discovery of noncanonical oligomeric states of N involving truncated C-terminal**
294 **domains**

295 Mononegavirus N molecules typically assemble into ring-like or helical structures. While
296 these canonical assemblies are well-characterized, alternative oligomeric states remain poorly
297 understood. To explore the full range of assembly possibilities, we sought to identify and
298 characterize highly unconventional oligomeric assemblies of BoDV-1 N that deviate
299 markedly from known architectures.

300 In addition to canonical ring-like structures, our cryo-EM analysis revealed highly
301 unconventional RNA-free complexes exhibiting S-shaped and triangular morphologies,
302 designated "S-shape-1", "S-shape-2", "Triangle-1", and "Triangle-2" (Fig. 4). These

303 complexes contain truncated N subunits composed solely of the C-terminal domain (N_{CTD}).
304 These act as bridging subunits connecting clusters of full-length N molecules, a configuration
305 not previously reported for other mononegaviruses.

306 Structural analysis identifies two unique inter-subunit interfaces in these assemblies (Fig.
307 4A): (1) a hydrophobic surface patch that is typically buried in full-length N becomes
308 exposed and mediates interaction between N_{CTD} subunits (Fig. 4B, S4C); and (2) polar loop
309 regions (residues 103–112 and 118–130) that form an additional contact site, potentially
310 involving electrostatic or hydrogen bonding interactions (Fig. 4C). These interfaces are
311 maintained across all distinct, novel RNA-free assemblies.

312 The cryo-EM density map of the octameric S-shape-1 complex shows that all full-length
313 subunits were connected via N-terminal arm domains (Fig. 4C). Notably, the connection
314 between the most spatially distant subunits features a highly flexible Gly-Gly-Ser sequence
315 (residues 39-41), located between the N-terminal arm and the core lobe of N, which permits a
316 pronounced bend between domains (Fig. 4C, S4D-E). The resulting modular architecture,
317 with distinct clusters bridged by full-length subunits, closely resembles that observed in
318 tetrameric and pentameric assemblies. This spatial correspondence suggests a domain-
319 swapping mechanism (Supplementary Fig. 4F), as observed in other mononegaviruses,
320 including vesicular stomatitis Indiana virus (VSIV)[7], measles virus[11], human
321 parainfluenza virus 5[30], and mumps virus[31].

322 SDS-PAGE analysis of highly concentrated, purified N samples from *E. coli* revealed a
323 prominent ~15-kDa band corresponding to the N_{CTD} fragment (Supplementary Fig. 4A).
324 Liquid chromatography-tandem mass spectrometry (LC-MS/MS) confirmed that this
325 fragment originates from cleavage at the boundary region between the N-terminal and C-
326 terminal lobes (Supplementary Fig. 4B).

327 Additionally, 3D reconstructions revealed two distinct assemblies composed of side-by-side
328 tetramers ("4-mer x2 parallel" and "4-mer x2 antiparallel") (Supplementary Fig. 4G, H). In
329 addition to these assemblies, 2D class averages also revealed cases in which a pentamer and a
330 tetramer, or a hexamer and a tetramer, appear nearby (Supplementary Fig. 1I). These
331 multimeric arrangements further support the idea that flexible inter-domain linkers enable
332 architectural transitions and may facilitate domain-swapping in BoDV-1 N.

333 **Virological importance of RNA-binding basic residues**

334 IB formation is a hallmark of many mononegavirus infections. In BoDV–1–infected cells,
335 these structures localize to the nucleus. Co-expression of N and P is sufficient to induce the
336 formation of IB-like structures in most mononegaviruses[32–36], including BoDV-1[37].
337 While our cryo-EM structures reveal how N recognizes RNA and assembles into ring-like
338 oligomers, they do not clarify whether RNA binding by N is strictly required for subsequent
339 steps in the replication cycle, such as RNA synthesis, and more specifically, formation of IBs.

340 To address this issue, we performed structure-guided alanine-scanning mutagenesis targeting
341 four key RNA-contacting residues of N: Lys154, Lys164, Arg297, and Arg321. Resulting
342 mutants, N(K154A), N(K164A), N(R297A), and N(R321A), were evaluated using a BoDV-1
343 minireplicon system and a nuclear IB reconstitution assay.

344 The minireplicon assay revealed that all four mutants were completely defective in
345 supporting viral RNA synthesis, indicating that these basic residues are essential for the
346 replication function of N (Fig. 5A). Furthermore, each mutation abolished the formation of
347 nuclear IB-like structures upon co-expression with the viral P in human cells (Fig. 5B).

348 These findings indicate that RNA binding by N is not only required for its replication
349 function, but also for forming biomolecular condensates involved in nucleocapsid assembly.

350 **Stable ring-like assemblies in the absence of RNA**

351 Nucleocapsid assembly has conventionally been considered RNA-dependent. However, the
352 precise contribution of RNA to the assembly of ring-like N oligomers in mononegaviruses,
353 including BoDV-1, remains unclear. To investigate whether BoDV-1 N can assemble into
354 ring-like structures in the absence of RNA, we analyzed mutants with diminished RNA-
355 binding capacity using single-particle cryo-EM.

356 We expressed and purified BoDV-1 N mutants, N(K154A), N(K164A), and N(R321A) in *E.*
357 *coli* (Supplementary Fig. 5A). The RNA content of purified mutant complexes was estimated
358 using their A260/A280 ratios, measured from SEC fractions corresponding to the elution
359 range of RNA-bound wild-type complexes. These ratios were 1.22 for N(K154A), 0.67 for
360 N(K164A), and 1.57 for N(R321A), compared to 1.36 for wild-type N. Although values vary
361 among mutants, they suggest differential levels of RNA association.

362 Subsequent cryo-EM analysis focused on the N(K164A) mutant, presumed to have the lowest
363 RNA-binding affinity. 3D reconstructions revealed various oligomeric assemblies that closely
364 resemble wild-type structures, but lack detectable RNA (Fig. 5C-N, S5B-E). The RNA-free
365 tetrameric structure closely matched the wild-type 4-mer-2 complex, with an RMSD of 0.62
366 Å, confirming that the Lys164Ala mutation does not disrupt protein folding (Fig. 5C-D).

367 Notably, RNA-free heptameric ring-like complexes, absent in wild-type preparations, appear
368 with other ring-like complexes exhibiting broader variations in circularity (Fig. 5M, N).
369 Triangular N_{CTD}-bridged complexes were not detected, possibly due to their low abundance.

370 These cryo-EM data demonstrate that BoDV-1 N has an inherent capacity to form
371 structurally diverse, RNA-free oligomers, including expanded ring-like architectures. This
372 implies that these rings arise from intrinsic self-assembly capacity of the N molecule, rather
373 than from RNA-mediated nucleation followed by dissociation, reinforcing the conclusion that
374 RNA binding is not a prerequisite for ring-like complex formation.

375 Discussion

376 Before this study, the BoDV-1 N–RNA complex was the only uncharacterized structure
377 among human mononegavirus families, highlighting the significance of these findings. Our
378 single-particle cryo-EM and functional analyses of the BoDV-1 N–RNA complex have
379 addressed this gap in the structural catalog of N molecules in the order *Mononegavirales*. Our
380 findings highlight evolutionary conservation across the *Mononegavirales*, while also
381 revealing lineage-specific adaptations that advance our understanding of nucleoprotein
382 biology. Extensive image classifications enable visualization of various conformational states
383 in solution, capturing both RNA-free and RNA-bound forms, including tetrameric,
384 pentameric, hexameric, larger ring-like assemblies, and non-canonical arrangements. These
385 states may fail to be detected by X-ray crystallography, which favors homogeneous, well-
386 ordered populations due to crystal packing. In contrast, cryo-EM reveals a broader
387 conformation ensemble that more closely reflects physiological diversity. The resolved
388 structures define key architectural principles of N oligomerization and correlate directly with
389 RNA encapsidation efficiency, as supported by structure-guided mutational analyses.
390 Collectively, they illustrate a previously unrecognized, stepwise assembly pathway for N–
391 RNA complexes (Fig. 6), in which N first oligomerizes independently of RNA, forming
392 intermediates that subsequently recruit RNA. Notably, this contrasts with canonical models in

which RNA initiates and guides N assembly, and instead supports a regulated pathway in which RNA-free intermediates act as checkpoints for genome encapsidation.

Ring-like N assembly and its implications

Ring-like N–RNA complexes have been observed in several mononegaviruses, including rhabdoviruses[7, 8] and pneumoviruses[10], before their biological relevance was fully understood. Subsequent studies confirmed that these assemblies share the same RNA-binding mode as helical nucleocapsids, demonstrating that they are not artifacts, but instead represent the fundamental principle of viral nucleocapsid formation[38–41]. Cryo-EM analyses of MuV N–RNA complexes revealed that N adopts nearly identical structures in ring-like and helical complexes (RMSD ~0.83 Å), and that ring-like structures can transition into helices upon exposure to cell-derived impurities[31]. This finding supports the idea that ring-like assemblies are structurally representative and potentially dynamically convertible intermediates. Cryo-electron tomography of HRSV-infected cells and virions further confirmed the presence of such ring-like assemblies in a native setting[42], highlighting their potential relevance during viral replication.

Our cryo-EM structural data demonstrate that BoDV-1 N forms stable ring-like assemblies, exhibiting key architectural features conserved among mononegavirus N proteins. These include extended N- and C-terminal arms that mediate inter-subunit interactions. The basic ring-like architecture is preserved across a spectrum of oligomeric forms, including hexamers, heptamers, and octamers, reflecting structural plasticity rather than a single dominant configuration (Fig. 2A-C). The observed variability in ring size and symmetry, together with the flexibility of polar interfaces and domain-swapping termini (Fig. 2H–J), suggests that these assemblies are modular and reversible intermediates capable of transitioning from ring-like to filamentous forms. Such plasticity may support dynamic reorganization of the nucleocapsid during different stages of the viral life cycle, such as replication, transcription, and packaging, and may reflect a conserved strategy across mononegavirus families.

Working assembly model of ring-like N–RNA complexes

Our cryo-EM analyses revealed unexpected structural diversity in BoDV-1 N assemblies, including symmetric and asymmetric complexes with varying RNA occupancy. These findings highlight a remarkable degree of conformational plasticity and suggest that these structures are not mere in vitro artifacts, but represent structurally and functionally relevant intermediates in nucleocapsid assembly. Based on the oligomeric states observed, ranging from RNA-free tetramers to RNA-bound hexamers and heptamers, we propose a working assembly model for BoDV-1 N–RNA complexes (Fig. 6 and Supplementary Movie 2).

In this model, BoDV-1 N initially forms RNA-free tetramers or pentamers. These assemblies act as precursors for subsequent fusion events, forming RNA-free S-shaped or triangular complexes involving the N_{CTD} and domain swapping of N-terminal arm domains. Subsequent removal of the N_{CTD}, along with domain-swapping of the C-terminal arm domain, may facilitate the formation of RNA-free hexameric and heptameric ring-like complexes.

Upon interaction with RNA, potentially facilitated by a chaperone-like polypeptide occupying the central channel, a local structural rearrangement occurs in the RNA-binding loop (residues 314–322), transitioning from a disordered state into a structured helix (Fig. 2I, 3D-G). This transition stabilizes RNA encapsidation in the inter-lobe cleft.

Inter-subunit interactions mediated by N- and C-terminal arm domains remain largely conserved between RNA-free and RNA-bound forms. However, RNA binding is associated with outward displacement of arm domains and reduced numbers of core domain contacts,

resulting in more open and flexible ring-like complexes, suitable to accommodate RNA strands. Repositioning of key residues such as Arg341 further supports stability of inter-subunit spacing (Fig. 2H-J).

Further research is required to validate this model experimentally. While the N_{CTD}-bridging mechanism appears to be stoichiometrically inefficient, likely sacrificing a subset of N molecules for structural transitions (Fig. 4), it may serve as a regulatory checkpoint during early stages of nucleocapsid formation by preventing uncontrolled oligomerization or non-specific RNA binding, thereby serving as a stable intermediate that promotes controlled and ordered nucleocapsid assembly.

Given that low-molecular-weight N-related products have also been observed in other mononegaviruses[15, 43], it would be useful to investigate whether truncated N contributes to N oligomerization in other members of the order.

Our structure-guided mutational analyses further support the notion that RNA binding occurs after formation of ring-like N oligomers. Mutations that disrupted RNA interaction do not prevent assembly of N complexes observed in the wild type (Fig. 5C–L), indicating that oligomerization can proceed independently of RNA binding. This implies a sequential assembly pathway in which N oligomerization precedes RNA encapsidation, allowing for regulated nucleocapsid formation. Such a mechanism could prevent premature or nonspecific RNA binding, ensuring that only properly assembled N oligomers participate in genome encapsidation.

Comparative understanding of N–RNA complex structures and assemblies in the order *Mononegavirales*

Mononegavirus N shares a conserved core architecture and function, yet the BoDV-1 N–RNA complex exhibits notable distinctions compared to those of *Paramyxoviridae*, *Pneumoviridae*, *Filoviridae*, and *Rhabdoviridae*. Structurally, all N proteins comprise two lobed domains that encapsidate the RNA genome in a positively charged cavity, protecting the genome and serving as the template for viral polymerase activity. BoDV-1 N follows this general blueprint, with a conserved RNA-binding loop that runs parallel to the RNA-binding cleft and that is critical for securing the genome. In BoDV-1 and filoviruses[16, 20], this loop undergoes a conformational change upon RNA binding (Fig. 2H, I, S3I, K, N, P), acting like a latch to lock the RNA in place. Mutations in the corresponding loop can impair RNA synthesis.

Although RNA recognition by N is nucleotide sequence-independent in BoDV-1 and other members of the *Mononegavirales*, relying on a network of backbone contacts rather than recognizing specific base identities, RNA positioning and stoichiometry of N molecules vary among families (Supplementary Table 3). BoDV-1 N encapsidates eight nucleotides per subunit, in contrast to six in the *Paramyxoviridae* and *Filoviridae*, seven in the *Pneumoviridae*, and nine in the *Rhabdoviridae*.

Another point of divergence is how N transitions from an RNA-free state to an RNA-bound oligomer and the role of the P molecule in that process. In most mononegaviruses, newly synthesized N proteins readily bind nonspecific RNA and self-assemble, requiring chaperoning by P to prevent premature RNA encapsidation[44, 45] and inappropriate oligomerization[13, 46]. BoDV-1 N, however, demonstrates exceptional stability in its RNA-free state and coexists with its RNA-bound state, as evidenced by our cryo-EM observations, suggesting reduced dependence on P for N oligomerization.

Evolutionarily, the mix of conserved and divergent features in N–RNA complexes among the *Mononegavirales* reflects their shared ancestry and long-standing functional constraints. The

core structural framework appears to be ancient and highly conserved, highlighting the enduring requirement of genome encapsidation. At the same time, divergence in nucleotide stoichiometry and assembly patterns seems to have emerged gradually, likely driven by lineage-specific constraints and neutral drift, possibly emerging from transient stochastic variation in early assembly mechanisms.

The BoDV-1 N–RNA complex, when compared with its paramyxo-, pneumo-, filo-, and rhabdovirus counterparts, provides a compelling case study of how different lineages in *Mononegavirales* may have independently explored alternative structural solutions while preserving core functionality.

In conclusion, our comprehensive structural and functional analyses of the BoDV-1 N molecule not only address a critical knowledge gap regarding mononegavirus N structures, but also provide insights into nucleocapsid assembly mechanisms. Our high-resolution cryo-EM structures of the BoDV-1 N–RNA complex reveal intricate details of binding interfaces and key residues mediating N-RNA interactions, identifying potential targets for antiviral therapeutics, particularly in the context of Borna disease. Furthermore, these findings contribute to a broader understanding of conserved N-RNA encapsidation and N-N interaction mechanisms throughout the order *Mononegavirales*. Our results provide not only a complete structural framework for mononegavirus N, but also a model of modular, regulated encapsidation that may extend to other members of the order. By illuminating these fundamental viral processes, our work supports future targeted interventions against BoDV-1 and enhances our preparedness for emerging mononegaviruses by revealing conserved structural features that could be exploited for broad-spectrum antiviral strategies.

Data Availability

The cryo-EM density maps and atomic coordinates have been deposited in the Electron Microscopy Data Bank (EMDB) and Protein Data Bank (PDB), respectively. For wild-type complexes, accession numbers are: EMD-61914 and PDB-ID 9JZI (4-mer-1); EMD-61915 and PDB-ID 9JZJ (4-mer-2); EMD-61916 and PDB-ID 9JZK (5-mer); EMD-61917 and PDB-ID 9JZL (6-mer); EMD-61918 (7-mer); EMD-61919 (8-mer); EMD-61920 (Flat 6-mer); EMD-61921 (Oval 6-mer-1); EMD-61922 (Oval 6-mer-2); EMD-61923 (S-shape-1); EMD-61924 (S-shape-2); EMD-61925 (Triangle-1); EMD-61926 (Triangle-2); EMD-61927 (4-mer x2 parallel); EMD-61928 (4-mer x2 antiparallel). For mutant N(K164A) complexes: EMD-61929 and PDB-ID 9JZN (4-mer); EMD-61930 (5-mer); EMD-61931 (6-mer); EMD-61932 (7-mer); EMD-61933 (Flat 6-mer); EMD-61934 (Oval 6-mer); EMD-61935 (Flat 7-mer); EMD-61936 (S-shape); EMD-61937 (Triangular 6-mer); EMD-61938 (4-mer x2 antiparallel). Cryo-EM raw images of wild-type N and mutant N(K164) have been deposited in the Electron Microscopy Public Image Archive (EMPIAR) with accession number EMPIAR-12716. Other data generated or analyzed during this study are available from the corresponding authors upon reasonable request.

Figure Legends

Fig. 1 Structures of RNA-free, ring-like N tetramers and pentamers

(A, B) Cryo-EM reconstructions of tetrameric ring-like N complexes in two conformations: (A) 4-mer-1 and (B) 4-mer-2. Subunits are uniquely colored in each structure. Left panels: side views; Right panels: bottom views. Square boxes indicate relative angles between the two lobes.

531 (C, D) Structural comparison of N subunit models between 4-mer-1 (grey) and 4-mer-2
532 (domain-colored as in Supplementary Fig. 1A). (C) Overall view of a subunit from inside of
533 the complex (Left) and from the bottom (right), highlighting major differences in the C-
534 terminal (CT) lobe and arm domains. (D) Close-up of inter-subunit region (dotted box in
535 panel C) showing flipped side chain of Arg341 and relative displacement of CT lobes (red
536 arrows).

537 (E) Cryo-EM reconstruction of 5-mer complex. Atomic models of N subunits (N_{1-5}) in warm
538 colors are superimposed on the cryo-EM map, forming an asymmetric pseudo-C5 structure
539 (orange frame) compared to a regular pentagon (dotted grey frame).

540 (F) Comparison of individual subunits within the pentamer, illustrating conserved core
541 domain (grey) and divergent NT and CT arms.

542 (G-I) Inter-subunit interactions in crystal structure (Xtal) (G), tetramers (4-mer-1, 4-mer-2)
543 (H), and pentamer (5-mer) (I). Surface representation of asymmetric subunit models with
544 interface clusters color-coded in four distinguishable pairs: (1) N-terminal arm (1-1: yellow)
545 and a shallow groove on N-terminal lobe (1-2: brown); (2) side area of N-terminal lobe (2-1:
546 pink, 2-2: red); (3) side area of C-terminal lobe (3-1: light green, 3-2: dark green); (4) C-
547 terminal arm (4-1: light blue) and a pocket on C-terminal lobe (4-2: dark blue). These cluster
548 numbers (1–4) correspond to the four types of N–N interaction interfaces described in the
549 main text. The comparison shows conserved interfaces in (1) and (4), and divergent interfaces
550 in (2) and (3). Scale bars: 20 Å.

551 **Fig. 2 Structures of ring-like N–RNA complexes and N-RNA interactions**

552 (A-C) Cryo-EM structure of the 6-mer (A), 7-mer (B), and 8-mer (C) ring-like N–RNA
553 complex reconstructed using C2, C1, and C2 symmetry, respectively. Asymmetric N subunits
554 are uniquely colored (white to blue), and RNA is shown in red. Scale bar: 20 Å.

555 (D) Atomic model of 6-mer complex in ribbon representation, built within the cryo-EM
556 density. Domains of N_1 subunit are color-coded as in Supplementary Fig. 1A.

557 (E) Tube representation of 6-mer model, highlighting gear-like RNA structure positioned
558 inside the ring (red).

559 (F) Close-up of N–RNA interface viewed from inside 6-mer ring, showing key basic amino
560 acid residues involved in binding eight RNA nucleotides. Side chains are depicted and
561 labeled as sticks.

562 (G) Schematic of RNA configuration and N-RNA interactions in the complex. Inward-facing
563 RNA bases (red), outward-facing RNA bases (green), and phosphate groups (orange) are
564 illustrated. Putative hydrogen bonds and electrostatic interactions between N residues and
565 RNA are shown as dashed lines.

566 (H) Structural comparison of N subunits from RNA-free tetramers (crystal structure, 4-mer-1,
567 4-mer-2, grey colors) and those from 6-mer (colored) shown in tube representation. Arrows
568 indicate major structural differences, color-coded by domain for the N_1 subunit. Dashed
569 boxes highlight the RNA-binding cleft (close-up in panel I) and the inter-subunit interface of
570 the C-terminal lobes (close-up in panel K).

571 (I) Close-up view of the RNA-binding cleft in ribbon representation, illustrating a local
572 structural transition in the C-terminal loop region to a helix (residues 314-322) upon RNA-
573 binding.

574 (J) Inter-subunit interfaces in 6-mer complex. Surface representation of asymmetric subunit
575 models, with interface clusters color-coded as in Fig. 1G. The RNA interface, highlighted in
576 orange. Scale bar: 20 Å.

577 (K) Close-up of Arg341 side chains of 6-mer complex and RNA-free tetramers, showing
578 flipping-in conformation, similar to that observed in 4-mer-2 (Fig. 1D).

579

580 **Fig. 3 Oval hexameric complexes with different circularity, with or without RNA and**
581 **additional volume in the center**

582 (A-C) Cryo-EM reconstructions of oval-shaped hexameric N complexes: (A) the most
583 elongated ring-like complex (Flat 6-mer), (B) an oval complex with extra central density
584 (Oval 6mer-1), and (C) oval complex with partial RNA density (Oval 6mer-2) reconstructed
585 with C1, C1, and C2 symmetry, respectively. Asymmetric subunits are uniquely colored
586 (white to blue) in all panels.

587 (D-G) Isolated cryo-EM maps of asymmetric N subunits, superimposed with atomic models
588 in ribbon representation: (D) Flat 6-mer, (E) Oval 6-mer-1, (F) Oval 6-mer-2, and (G) RNA-
589 bound 6-mer (reference for RNA cryo-EM density). For oval complexes, the tetramer (4-mer-
590 2) atomic model was initially fit as a rigid body, and then flexibly fit using molecular
591 dynamics flexible fitting (MDFF) as implemented in ISOLDE[47], within UCSF ChimeraX.

592 **Fig. 4 S-shaped and triangular complexes containing N-terminally truncated bridging**
593 **subunits**

594 Cryo-EM reconstructions of N complexes composed of full-length N molecules bridged by
595 N_{CTD} (C-terminal domain only). Each asymmetric subunit is color coded: full-length in blue
596 tones, and N_{CTD} in warm colors (e.g., orange or red).

597 (A) "S-shape-1": two trimeric units bridged by an N_{CTD} pair.

598 (B) Close-up of the interface between an N_{CTD} pair, showing direct interaction at the bridging
599 site.

600 (C) Close-up of the interface formed by an N-terminal arm, highlighting a distinct inter-
601 subunit contact.

602 (D) "S-shape-2": a trimer and a tetramer bridged by an N_{CTD} pair, arranged asymmetrically.

603 (E) "Triangle-1": three dimers arranged in a triangle and bridged by three N_{CTD} pairs along
604 each edge of the triangle.

605 (F) "Triangle-2": two dimers and a trimer bridged by three pairs of CTDs, again bridged by
606 three N_{CTD} pairs.

607 Scale bars: 50 Å.

608

609 **Supplementary Fig. 5 Purification and structural analysis of N mutants**

610 (A) SEC profiles for N mutants: N(K154A), N(K164A), and N(R321A). Arrows indicate
611 fractionation zones, with a cyan arrow marking the fraction subjected to cryo-EM analysis.

612 (B) Representative cryo-electron micrographs of purified N(K164A) complexes from
613 fractions that eluted earlier. Scale bar: 50 nm.

614 (C) Workflow of the single-particle cryo-EM analysis performed for N(K164A) complexes.

615 (D) Representative 2D class averages of N(K164A), demonstrating structural heterogeneity
616 and pleomorphism. Scale bar: 20 nm.

617 (E) Resolution estimation plots for cryo-EM reconstruction. Red curve: gold-standard FSC
618 between independent half-maps (threshold at FSC = 0.143). Black curve: FSC between the
619 full cryo-EM map and the atomic model (threshold at FSC = 0.5). Local resolution maps are
620 shown in each panel, with color scales ranging from blue to red in Å, as indicated by the bar.

621 **Fig. 5. Structure-guided mutational assays**

622 (A) Viral polymerase activity assessed by minireplicon assay using wild-type (WT) and
623 mutant BoDV-1 N. Activity is shown as the ratio of *Gaussia* luciferase (Gluc) to *Cypridina*
624 luciferase (Cluc) relative light units (RLU), normalized to 1.0 for the negative control [L (-)].
625 Mutations K154A, K164A, R297A, and R321A all caused marked reduction in activity.
626 Statistical analysis was not performed due to consistently severe activity loss in all mutants.

627 (B) Subcellular localization of WT or mutant N(K154A, K164A, R297A, or R321A) co-
628 expressed with WT P in U-2 OS cells, analyzed by confocal immunofluorescence
629 microscopy. Left panels: BoDV-1 P (grey); Center panels: BoDV-1 N (grey); Right panels:
630 merged images (N: red, P: green, and nuclei: blue). White arrowheads highlight nuclear IB-
631 like structures co-occupied by both N and P. Scale bars: 5 μm.

632 (C-M) Cryo-EM reconstructions of the N(K164A) reveal diverse oligomeric states. Colored
633 maps represent different structural classes: green for WT-like, yellow for WT-like, but
634 lacking RNA density, and orange/red for structures distinct from WT.

635 (C) Tetrameric (4-mer) structure of N(K164A) with an atomic model overlay. Subunits are
636 uniquely colored.

637 (D) Structural superposition of N(K164A) and WT 4-mer models in wire representation,
638 showing high overall similarity.

639 (E–H) Additional assemblies of N(K164A): (E) 5-mer, (F) S-shape complex, (G) Flat 6-mer,
640 and (H) 4-mer x2 antiparallel. Left panels: mutant maps; right panels: map-to-map
641 comparisons with WT (white).

642 (I) WT 6-mer cryo-EM map with rigid-body fitted model (N: Chain B, white; RNA: Chain R,
643 red). The fitted model confirms the presence of RNA in the binding cleft, serving as a
644 reference for RNA localization in subsequent comparisons.

645 (J–L) Ring-like assemblies of N(K164A): (J) 6-mer, (K) 7-mer, and (L) Oval 6-mer. Left
646 panels: mutant map; Center panels: map-to-map comparison with the WT (white); right
647 panels: map-to-model comparison using the WT N–RNA complex model (protein: white,
648 RNA: red). Core domains of WT model (Chain B of 6-mer) were rigid-body fitted into each
649 subunit region to assess RNA occupancy. In all structures, the RNA-binding cleft lacked
650 corresponding density, and fitted RNA models protrude from the map, indicating loss of
651 RNA binding.

652 (M, N) N(K164A)-specific assemblies: (M) Flat 7-mer and (N) Triangular 6-mer ring-like
653 complexes. Left panels: mutant maps; right panels: map-to-model comparison using the WT
654 N–RNA complex model (protein: white, RNA: red). Map-to-map comparison with WT was
655 not performed, as no equivalent conformations were observed in the WT dataset. As observed
656 in panels J–L, the RNA-binding cleft lacked density, as evidenced by RNA models
657 protruding outside the cryo-EM map.

658 **Fig. 6. A model of ring-like N–RNA complex assembly**

659 Cryo-EM analysis of BoDV-1 N protein reveals diverse oligomeric states, representing
660 potential intermediate stages in nucleocapsid assembly. The model begins with RNA-free
661 tetrameric or pentameric complexes, which serve as initial oligomerization cores. These
662 structures may undergo fusion and reorganization, giving rise to asymmetric intermediates
663 such as S-shaped and triangular assemblies, involving domain swapping and transient N_{CTD}
664 bridging. Subsequent removal of N_{CTD} and structural realignment of arm domains lead to
665 forming ring-like hexamers and heptamers. Upon RNA binding, a local loop-to-helix
666 transition is induced in the C-terminal lobe (residues 314–322), stabilizing RNA
667 encapsidation. The final structure is a fully assembled RNA-bound hexamer, with
668 coordinated inter-subunit arm interactions and well-positioned RNA in the inter-lobe clefts.
669 This model illustrates the stepwise and flexible nature of BoDV-1 nucleocapsid assembly,
670 integrating both RNA-free self-assembly and RNA-guided structural stabilization.

671 Supplementary Information

672 **Supplementary Table 1. Cryo-EM analysis and atomic model building for wild-type N**

673 **Supplementary Table 2. Cryo-EM analysis and atomic model building for N(K164A)**

674 **Supplementary Table 3. Comparative structural features of N–RNA complexes across**
675 **families in the order *Mononegavirales***

676 **Supplementary Fig. 1. Expression, purification, and cryo-EM analysis of BoDV-1 N**
677 **complexes**

678 (A) Schematic of BoDV-1 N domain organization. Bold boxes indicate regions rich in
679 secondary structure. Domain colors for the N-terminal (NT) arm, NT lobe, C-terminal (CT)
680 lobe, and CT arm are consistent across all figures.

681 (B) Size-exclusion chromatography profile of the purified BoDV-1 N complex. Two peaks
682 were fractionated (#1 and #2), with SDS-PAGE analysis shown for each. These fractions
683 were used for subsequent cryo-EM analyses.

684 (C) Representative cryo-EM micrograph (left) and 2D class averages (right) of complexes
685 from the #2 fraction. Data were acquired on a 200-kV Glacios cryo-TEM and analyzed with
686 RELION4-beta. Scale bars: 50 nm (left) and 50 Å (right).

687 (D) 2D projections of the crystal structure (PDB ID: 1N93) simulated at 9 Å resolution for
688 visual comparison, using the molmap command in UCSF Chimera X and the
689 relion_projection command. Scale bar: 50 Å.

690 (E) Representative cryo-EM micrograph (left) and 2D class averages (right) of N complexes
691 from the #1 fraction. The left image was acquired using a 200-kV Glacios cryo-TEM, and the
692 right image represents the results of image analysis performed on data collected with a 300-
693 kV Titan Krios microscope, processed using cryoSPARC. Scale bars: 50 nm (left), 50 Å
694 (right).

695 (F) Workflow of single-particle cryo-EM analysis for N complexes in #1 fractions. Particles
696 in cryo-EM images were picked, classified, and refined to generate 3D reconstructions. These
697 fractions contained a mixture of oligomeric states, including tetramers (4-mers), pentamer (5-
698 mer), hexamers (6-mers), heptamer (7-mer), octamers (8-mer, S-shape-1), nonamers (9-mer,
699 S-shape-2), dodecamers (Triangle-1: 12-mer), and complex composed of 13 subunits
700 (Triangle-2: 13-mer). Although the nonameric ring-like complex (9-mer) was observed in

raw micrographs and 2D class averages, a corresponding 3D reconstruction could not be obtained, due to its sparse representation among the sampled assemblies. Fifteen cryo-EM maps were reconstructed in the box shown in color at the bottom. In that box, the name of each map (applied symmetry), overall resolution, and the number of particles used (ptcls) are provided. Blue and red boxes represent RNA-free and RNA-bound complexes, respectively.

(G) FSC plots for resolution assessment: between independently refined half maps (half maps, red) and full cryo-EM reconstruction and the atomic model (map vs model, black). Thresholds: 0.143 (half maps) and 0.5 (map vs model). Local resolution maps are shown with color scales from blue to red (Å).

(H) Expression and purification of BoDV-1 N complexes from HEK293T cells. Left: SDS-PAGE after Ni-NTA affinity purification. Middle: negative-stain electron micrograph. Right: zoomed-in view of ring-like structures indicated by the arrows in the middle panel. These are consistent with complexes observed in the *E. coli* system. Scale bars: 50 nm (middle) and 10 nm (right).

(I) Representative 2D class averages showing oligomer pairs in proximity: a pentamer with a tetramer ("5-mer + 4-mer", top panel) and a hexamer with a tetramer ("6-mer + 4-mer", bottom panel). Scale bar: 10 nm.

Supplementary Fig. 2. Structural comparisons and local resolution of cryo-EM maps

(A) Left and Middle panels: bottom views of 4-mer-1 and 4-mer-2. Right panel: Schematic illustrating the angular difference between C-terminal and N-terminal lobes.

(B) Structural alignment of 4-mer-1 (colored) with crystal structure (Xtal, transparent grey). Atomic models are shown as Cα backbone wire representations. The crystal structure exhibits a more compact conformation.

(C-E) Local resolution maps of cryo-EM reconstructions for (C) 4-mer-1, (D) 4-mer-2, and (E) 5-mer complexes. For tetramers: complete complex maps (left panel) and segmented asymmetric subunit maps (right panels). Color scale ranges from blue to red (Å), as indicated by the color bar.

(F-H) Atomic models colored by *B*-factor for (F) 4-mer-1, (G) 4-mer-2, and (H) 5-mer. The color scale ranges from blue (low *B*-factor, indicating more stable regions) to red (high *B*-factor, indicating more flexible regions) in $Å^2$, as indicated by the color bar. In (H), a close-up view highlights the region with the highest *B*-factors (dotted boxes); amino acid numbers of the N-terminal arm are shown in the right panel.

(I, J) 6-mer complex: (I) Local resolution map and (J) atomic model colored by *B*-factor. Color scales are the same as in panels (C-H).

Supplementary Fig. 3. RNA structures in viral N–RNA complexes in the order *Mononegavirales*

(A-E) Atomic models of representative N–RNA complexes from five families in the *Mononegavirales*, shown in surface representation. RNA is depicted in red using a ladder representation in the top view to highlight the configuration of the RNA backbone and base arrangement: (A) measles virus (MV, PDB-ID 4UFT[11]) and parainfluenza virus 5 (PIV5, PDB-ID 4XJN[30]), *Paramyxoviridae*; (B) Human respiratory syncytial virus (HRSV, PDB-ID 2WJ8[10]) and human metapneumovirus (HMPV, PDB-ID 5FVC[15]), *Pneumoviridae*; (C) Ebola virus (EBOV, PDB-ID 5Z9W[16]) and lloviu virus (LLOV, PDB-ID 7YPW[21]), *Filoviridae*; (D) vesicular stomatitis Indiana virus (VSIV, PDB-ID 2GIC[7]) and Rabies virus (RABV, PDB-ID 2GTT[8]), *Rhabdoviridae*; (E) BoDV-1 (6-mer, PDB-ID 9JZI, this study),

Bornaviridae. For the heptameric and octameric N–RNA complex, the NT-arm, core, and CT-arm of a subunit in the hexameric model are independently fitted into cryo-EM maps as rigid bodies.

(F) Amino acid sequence alignment of the N molecules from members in the genus *Orthobornavirus*: Borna disease virus 1 (BoDV-1, Uniplot: UPO09291.1), Borna disease virus 2 (BoDV-2, Uniplot: YP_009268917.1), estrildid finch bornavirus 1 (EsBV-1, Uniplot: YP_009505423.1), variegated squirrel bornavirus 1 (VSBV-1, Uniplot: YP_009269413.1), Loveridge's garter snake virus 1 (LGSV-1, Uniplot: YP_009055058.1), and parrot bornavirus 7 (PaBV-7, UniProt: YP_009268899.1). Conserved and similar residues are highlighted with filled and hollow boxes, respectively. Blue arrowheads indicate positions of RNA-binding basic residues. Secondary structure assignments are shown for the N protein in the RNA-free 4-mer-1 (PDB-ID 9JZJ) and the RNA-bound 6-mer (chain B, PDB-ID 9JZL). Solid lines denote modeled regions, dotted lines indicate unmodeled regions, and dots mark alignment gaps. Alpha helices and beta sheets are indicated by coils and arrows, respectively. Domain colors follow the scheme in Supplementary Fig. 1A.

(G-K) Conformational shift and RNA-binding motifs of N molecules among members of the order *Mononegavirales*. In each panel, the RNA-bound state (color) is overlaid with the RNA-free state (grey) to facilitate structural comparison. (G) MV (N–RNA, PDB-ID 4UFT; N0-P, PDB-ID 5E4V[12]), PIV-5 (N–RNA, PDB-ID 4XJN; N0-P, PDB-ID 5WKN[48]) and Nipah virus (NiV; N–RNA, PDB-ID 7NT5[24]; N0-P, PDB-ID 4CO6[49]), *Paramyxoviridae*. (H) HMPV (N–RNA, PDB-ID 5FVC; N0-P, PDB-ID 5FVD[15]), *Pneumoviridae*. (I) EBOV (NP–RNA, PDB-ID 5Z9W[16]; NP0-VP35, PDB-ID 4YPI[14]) and Marburg virus (MARV; NP–RNA, PDB-ID 7F1M[20]; NP0-VP35, PDB-ID 5F5M), *Filoviridae*. (J) VSIV (N–RNA, PDB-ID 2GIC; N0-P, PDB-ID 3PMK[50]) and RABV (N–RNA, PDB-ID 8FFR[17]; N0-P, PDB-ID 8B8V[17]), *Rhabdoviridae*. (K) BoDV-1, Bornaviridae. Note: In filoviruses, nucleoprotein and phosphoprotein are conventionally abbreviated to NP and VP35, respectively.

(L-P) Schematic diagrams corresponding to panels (G-K), with annotated text highlighting key structural differences between RNA-free and RNA-bound states for each virus.

(Q-U) Close-up of N–RNA binding interface for: (Q) MV, (R) HMPV, (S) EBOV, (T) RABV, and (U) BoDV-1. Blue dashed lines indicate residues within hydrogen bond distance. RNA and RNA-binding loops are colored and labeled, whereas other regions of the protein are rendered in translucent white for clarity.

Supplementary Fig. 4. Complex assemblies and unique protein-protein interactions involving N_{CTD}

(A) Purification and characterization of BoDV-1 N protein. Left: SEC profile of purified BoDV-1 N protein. Blue dashed lines indicate fractions for further analysis. Right: SDS-PAGE of SEC fractions. A band distinct from full-length N (arrow) was excised from Fraction #2 and analyzed by LC-MS/MS.

(B) LC-MS/MS analysis of BoDV-1 N protein (Q Exactive Plus, Thermo Fisher Scientific). Samples were digested with trypsin or chymotrypsin. Top: Histogram showing peptide coverage across the N protein sequence. Bottom: Detected amino-acid sequences and their counts in the boundary region between the C-terminal and N-terminal lobes. Residues presumed to have been cleaved at the carboxy terminus by protease are highlighted in grey. Putative CTD cleavage sites were identified at positions 214D-215F, 220K-221E, and 222F-223M.

(C) Binding interface between the cleaved N_{CTD} in the S-shape-1 complex. Top: Surface representation of the S-shape-1 complex, with bridging subunits N_4 and N_8 highlighted in pink. The red outline indicates the area enlarged in the lower panels. Bottom: hydrophobic/hydrophilic surface potential of the outlined region, calculated using the Brasseur method[51], colored cyan (hydrophilic) and orange (hydrophobic).

(D, E) Structural comparison of subunits from the S-shape-1 and 4-mer-1. (D) N-terminal arm in the S-shape-1 complex exhibits a sharp bend, (E) centered at a Gly-Gly-Ser motif (residues 39-41).

(F) Spatial arrangement of subunits in the S-shaped, triangular complexes. Atomic models of tetrameric complexes (cool colors) and pentameric complexes (warm colors) are superimposed to show well-aligned architecture. Scale bar: 50 Å.

(G, H) Tetrameric complexes aligned in (G) parallel and (H) antiparallel configurations. Scale bar: 50 Å.

Supplementary Movie 1. Visualization of continuous conformational heterogeneity in BoDV-1 N complexes

3D Variability Analysis in CryoSPARC revealed the continuous conformational landscape of the N complexes. Animation cycles through seven distinct assemblies of N complexes. This approach complemented the distinct assembly states identified by 3D classification, revealing structural heterogeneity that suggests continuous conformational changes within each state. Scale bar: 10 Å.

Supplementary Movie 2. An assembly model of the hexameric ring-like N–RNA complex

This morph movie illustrates a possible assembly pathway of the BoDV-1 N–RNA complex, starting from an RNA-free tetramer and sequentially transitioning through a twin tetramer, an S-shaped complex, a flat hexamer, an oval hexamer, and finally a fully assembled ring-like hexamer bound to RNA. Dynamic transformations highlight the structural plasticity of the N protein and suggest potential intermediates in nucleocapsid assembly, providing insights into possible stepwise assembly of the functional N–RNA complex.

Materials and methods

Protein expression and specimen purification

Expression and purification of the full-length N protein of the Borna disease virus 1 (the species *Mammalian 1 orthobornavirus*, Uniplot: P0C796) was conducted with *E. coli* and mammalian expression systems.

For the *E. coli* expression system, an N-terminal hexahistidine-tagged N was expressed in Rosetta™ 2(DE3) pLysS competent cells (71403; Novagen, Inc., Madison, WI, USA) through induction with 0.5 mM isopropyl β- d-1-thiogalactopyranoside at 16 °C overnight. Pelleted cells were resuspended in a sonication buffer: Tris buffer (20 mM Tris-HCl, pH 7.4, 150 mM NaCl) containing 10 mM imidazole and a protease inhibitor cocktail (25955-24; Nacalai Tesque, Inc., Japan). After sonication, lysates were clarified by centrifugation at 20,000 × g for 10 min at 4 °C. Then, supernatants were loaded onto a column containing TALON® Metal Affinity Resin (635501; Takara Bio, Inc., Shiga, Japan). Resin was washed with sonication buffer, and histidine-tagged proteins were eluted with sonication buffer containing 300 mM imidazole. Samples were then applied to size-exclusion chromatography using a Superdex 200 Increase10/300 GL column (Cytiva, USA) in Tris buffer. Fractions

836 were concentrated with Amicon® Ultra Centrifugal Filters (Merck KGaA, Darmstadt,
837 Germany) and stored at 4°C. Samples were subjected to mass spectrometry, negative-stain
838 transmission electron microscopy (TEM), and cryo-EM analysis.

839 For the mammalian expression system, human embryonic kidney 293T (HEK 293T) cells
840 were transfected with a pCAGGS plasmid coding the full-length N protein with an N-
841 terminal hexahistidine tag. Three days post-transfection, cell pellets were resuspended and
842 gently mixed on ice for 15 min in lysis buffer: Tris buffer containing 0.05% NP-40 substitute
843 (Wako, 141-08321), a protease inhibitor cocktail (EDTA-free) (Roche, 11836170001), and 2
844 mM Ribonucleoside-Vanadyl Complex (NEB, S1402S). Insoluble components were pelleted,
845 and supernatant was collected and mixed with pre-equilibrated TALON® Metal Affinity
846 Resin (TaKaRa, 635502) and incubated on ice for 20 min, followed by two washes with
847 binding buffer, Tris buffer containing 10 mM imidazole, and pelleting of the resin. The resin
848 was loaded onto a column, and histidine-tagged proteins were eluted with elution buffer: Tris
849 buffer containing 500 mM imidazole. Eluted samples were subjected to negative-stain TEM
850 to compare assembly of N complexes in different expression systems.

851 **Negative-stain transmission electron microscopy**

852 A 5-µL aliquot of the specimen was applied to freshly glow-discharged, carbon-coated 600-
853 mesh copper grids (Gilder Grids Ltd, UK). After allowing samples to adhere for 1 min,
854 excess liquid was gently blotted away using filter paper. Subsequently, grids were
855 immediately stained with three drops of 2% (w/v) phosphotungstic acid, adjusted to pH 7.0.
856 After carefully removing excess staining solution, grids were air-dried at room temperature
857 before imaging. Imaging was conducted on an HT-7700 transmission electron microscope
858 (Hitachi High-Tech, Japan) at an acceleration voltage of 80 kV, using an XR81-B CCD
859 camera (Advanced Microscopy Techniques, USA).

860 **Cryo-EM specimen preparation and data acquisition**

861 A 2-µL aliquot of specimen solution was applied twice onto glow-discharged Quantifoil
862 R1.2/1.3 Gold 300 mesh grids (Quantifoil Micro Tools GmbH, Germany). After blotting
863 excess solution on the grids with filter paper, specimens were rapidly frozen in liquid ethane
864 on a Vitrobot Mark IV (Thermo Fisher Scientific, USA). Cryo-grids were initially screened
865 using a Glacios cryo-TEM (Thermo Fisher Scientific, USA) operated at an acceleration
866 voltage of 200 kV, equipped with a Falcon4 direct electron detector at the Institute for Life
867 and Medical Sciences, Kyoto University.

868 Cryo-EM data from wild-type N were collected on a pre-screened cryo-grid on a Titan Krios
869 cryo-TEM operated at 300 kV (Thermo Fisher Scientific, USA), equipped with a Cs corrector
870 (CEOS GmbH, Germany) at the Institute for Protein Research, Osaka University. Image
871 acquisition was performed using a beam-image shift scheme with a 3 × 3 hole configuration
872 with two target positions per hole using the SerialEM software[52] with a nominal defocus
873 range of −0.6 to −1.6 µm in EFTEM nanoprobe mode. Images were acquired as 60-frame
874 movies using a Gatan BioQuantum energy filter with a slit width of 20 eV and a K3 direct
875 electron detector (Gatan, Inc., USA) in the electron-counting and correlated double sampling
876 (CDS) imaging mode. 29,340 movies were acquired at a dose rate of 9.0 e^-/pixel/s, a pixel
877 size of 0.88 Å, and a cumulative exposure of 40 $e^-/Å^2$. Detailed imaging conditions are
878 described in Supplementary Supplementary Table 1.

879 Cryo-EM data from the N(K164A) were collected on a pre-screened cryo-grid on a Glacios
880 cryo-TEM equipped with a Falcon4 camera (Thermo Fisher Scientific, USA) operated at 200
881 kV at the Institute for Life and Medical Sciences, Kyoto University. Image collection was
882 conducted using aberration-free image shift (AFIS) capability managed with EPU software

(Thermo Fisher Scientific, USA) with a nominal defocus range of −0.6 to −1.6 μm in nanoprobe mode with electron event representation (EER) mode. 5,733 movies were acquired at a dose rate of 9.0 e^-/pixel/s, a pixel size of 0.724 Å, and a cumulative exposure of 43 $e^-/Å^2$. Detailed imaging conditions are described in Supplementary Table 2.

Cryo-EM image processing

For the wild-type N dataset, acquired images were chronologically split into six subsets. Gain reference images were generated for each subset using all movie frames with "relion_estimate_gain" command in RELION4-beta[53]. Subsequent image processing was performed using the software cryoSPARC[54, 55]. Motion correction and gain normalization were carried out using "Patch motion correction", and the contrast transfer function (CTF) was estimated using "Patch CTF Estimation". Particle coordinates were registered with Topaz using the pre-trained model ResNet16 (64 units)[56], and selected particles were extracted into a 140×140-pixel box with a pixel size of 2.64 Å (binning 4). These particles were subjected to four rounds of 2D classification to remove low-quality particles and to assess and identify diverse, complex structures. Selected particles were then subjected to reference-free 3D reconstruction using "Ab-initio Reconstruction" to generate 3D initial maps. Reference-based 3D classification was performed using "Heterogeneous Refinement" to classify complex structures roughly. A subsequent round of 2D classification was performed to analyze particle population heterogeneity further and to remove remaining contaminants and low-quality particles. Classes containing heterogeneous structures from six subsets were combined and subjected to a subsequent reference-based 3D classification using "Heterogeneous Refinement". This step was necessary as most classes still contained a mixture of molecules with varying oligomeric states or conformations. These subsets were categorized as follows: "4-mers", "5-mer and Flat 6-mer", "6-mer", "Oval 6-mers", "7-mer, 8-mer", and "S-shapes, and Triangles" classes. Resulting subsets were subjected to further 3D classification and particle sorting using multiple rounds of "Ab-initio Reconstruction". This step effectively removed remaining low-quality particles and improved class homogeneity. Concurrently, structural heterogeneity of each complex was visualized and evaluated using "3D Valiability" during 3D classification (Supplementary Movie 1). Final reconstructions were obtained using either "Homogeneous Refinement" or "Non-uniform Refinement". A detailed image processing workflow is depicted in Supplementary Fig. 1E.

For the N(K164A) dataset, gain reference images were generated for each subset using all movie frames with "relion_estimate_gain" command in RELION4-beta. Subsequent image processing steps were conducted using cryoSPARC. The CTF was estimated using the "Patch CTF Estimation". Particle coordinates were registered with "Blob Picker", and selected particles were extracted into a 210×210-pixel box with a pixel size of 1.448 Å (binning 2). These particles were subjected to several rounds of 2D classification to remove low-quality particles and to assess and identify diverse, complex structures. Selected 2D classes were employed as references, and "Template Picker" was conducted. Particles were re-extracted, classified, and selected in the same manner, and selected particles were then subjected to reference-free 3D reconstruction using "Ab-initio Reconstruction" to generate 3D initial maps. Reference-based 3D classification was performed using "Heterogeneous Refinement" to classify complex structures roughly. Another 2D classification was performed to examine what structures were mixed and to remove additional low-quality particles. Structures with high similarity were grouped and subjected to another reference-based 3D classification using "Heterogeneous Refinement" since most of classes were yet a blend of molecules with varying numbers of subunits or conformations, namely "4-mers", "5-mer and S-shape", "6-mers", and "7-mers" classes. Classified structures and particles were subjected to final 3D

931 reconstruction using “Homogeneous Refinement” and “Non-uniform Refinement” (only for
932 4-mers). A detailed image processing workflow is depicted in Supplementary Fig. 5C.

933 **Atomic model building and refinement**

934 RNA-free N (PDB-ID 1N93) was used as the starting model, fitted as a rigid body into cryo-
935 EM maps using UCSF ChimeraX[57]. The model was then manually adjusted to fit the map
936 with *Coot*[58]. RNA was modeled de novo as uracil nucleotides using *Coot*. These models
937 were refined with *REFMAC5*[59] in *Servalcat*[60], employing external restraints generated
938 with *ProSMART*[61] and *LIBG*[62]. RNA-free tetramers (4-mer-1 and 4-mer-2) and RNA-
939 bound hexamer (6-mer) models were refined with C4 and C2 symmetry constraints,
940 respectively, consistent with the symmetry imposed during cryo-EM reconstruction.

941 **Nuclear inclusion body reconstitution assay**

942 U-2 osteosarcoma (OS) cells (92022711; European Collection of Authenticated Cell
943 Cultures, Public Health England, London, England) were cultured in Dulbecco's Modified
944 Eagle Medium (DMEM) (08456; Nacalai Tesque, Inc., Japan) supplemented with 10% fetal
945 bovine serum. For transfection, cells were seeded on coverslips in 24-well culture plates and
946 co-transfected with 250 ng of plasmid DNA encoding BoDV-1 N and 25 ng of plasmid DNA
947 encoding BoDV-1 P using polyethylenimine "Max" (24765-1; Polysciences, Inc.,
948 Warrington, PA, USA). At 24 h post-transfection, cells were fixed with 4%
949 paraformaldehyde for 10 min, permeabilized, and blocked with 5% bovine serum albumin
950 containing 0.5% Triton X-100 for 15 min. Viral proteins in these cells were then probed with
951 primary antibodies for 2 h at room temperature (RT), followed by two washes with
952 phosphate-buffered saline (PBS). Subsequently, cells were incubated with secondary
953 antibodies and 4′,6′-diamidino-2-phenylindole (DAPI) for 1 h at RT, washed three times with
954 PBS, and mounted with ProLong® Diamond Antifade Reagent (Life Technologies, P36961).
955 Immunofluorescence images were acquired using a laser scanning confocal microscope
956 (LSM 700; Carl Zeiss AG, Switzerland) equipped with a Plan-Apochromat 63× objective
957 lens (numerical aperture = 1.4). The following antibodies were used in this study: anti-
958 BoDV-1 N mouse monoclonal antibody (HN132), anti-BoDV-1 P rabbit polyclonal antibody
959 (HB03), goat anti-mouse IgG (H+L) highly cross-adsorbed secondary antibody conjugated
960 with Alexa Fluor 568 (A-11031; Thermo Fisher Scientific), goat anti-rabbit IgG (H+L)
961 highly cross-adsorbed secondary antibody conjugated with Alexa Fluor 488 (A-11034;
962 Thermo Fisher Scientific).

963 **Minireplicon assay**

964 For the minireplicon assay, 1.6×10^5 of 293T cells were seeded onto 24-well plates. The
965 following day, cells were transfected with 150 ng of minigenome plasmid possessing the
966 *Gaussia* luciferase (Gluc) gene as a reporter[63], 150 ng of pCAGGS-N (wild-type or
967 mutants), 150 ng of pCAGGS-L, 15 ng of pCAGGS-P, and 35 ng of a control plasmid
968 expressing secreted *Cypridina* luciferase (Cluc) under the control of an SV40 promoter
969 (pSV40-Cluc), using Avalanche®-Everyday Transfection Reagent (EZ Biosystems). At 72 h
970 post-transfection, culture supernatants were subjected to luciferase assays using Pierce™
971 Gaussia Luciferase Glow Assay Kit and Pierce™ Cypridina Luciferase Glow Assay Kit
972 (Thermo Fisher Scientific). Polymerase activity was quantified by normalizing Gluc activity
973 to Cluc activity, an internal control for transfection efficiency.

974 **Data visualization**

975 Molecular visualizations and structural representations were generated using UCSF Chimera
976 X (version 1.8)[57]. Plots and graphs were created using gnuplot (version 6.0)[64]. Multiple
977 sequence alignments of N were performed using MAFFT[65] with default parameters.

Resulting alignments were visualized and formatted using the ESPript3 server[66]. All figures were assembled, formatted, and annotated using Adobe Illustrator (version 28.7.1) to ensure consistent style and labeling.

Quantification and Statistical Analysis

Cryo-EM image processing and model building were performed using standard single-particle analysis methods. 3D reconstruction and resolution estimation were based on the "gold-standard" Fourier shell correlation using the 0.143 criterion, where two independently refined half-sets of the data are compared to minimize reference bias. Quality of final atomic models was assessed using *MolProbity*. The model-to-map fit was evaluated using *Servalcat* software.

Fluorescence microscopy data were obtained from multiple independent experiments, and representative images were shown. Observed patterns were consistent among all replicates, confirming reproducibility of results. To ensure comparability, image acquisition settings were kept consistent among all samples in each experiment.

Minireplicon assays were performed in technical duplicates across three independent biological replicates. These measurements showed a stark contrast between wild-type and mutant samples. Negative control, L(-), values consistently ranged from 1/90 to 1/170 of wild-type measurements, with mutant samples exhibiting values comparable to those of negative controls. Given the magnitude and consistency of these differences among all replicates, where mutant values were indistinguishable from background levels, the biological significance of observed differences is evident from the raw data, and formal statistical analysis was deemed unnecessary.

Acknowledgments

We thank Mika Hirose and Takayuki Kato (Institute for Protein Research, Osaka University) for managing and providing user support at their cryo-EM facility; Yuzo Watanabe (Proteomics Facility, Graduate School of Biostudies, Kyoto University) for assistance with the mass spectrometry analysis, Steven D. Aird for editing the manuscript, and Yoshihiro Kawaoka for fruitful discussions. This work was supported by Grant-in-Aid for the Ministry of Education, Culture, Sports, Science and Technology (MEXT) Leading Initiative for Excellent Young Researchers; Japan Society for the Promotion of Science (JSPS) Scientific Research (C) (21K07052); JSPS Transformative Research Areas (B) (21H05117); Japan Science and Technology Agency (JST) FOREST Program (JPMJFR214S); research grant from the Kazato Research Encouragement Prize (to YS); JSPS Scientific Research (C) (23K06574 to YH) and (B) (21H01199, 23K20902 to MH, and 24K02284 to YS, YH, and MH); JSPS Core-to-Core Program A, Advanced Research Networks (JPJSCCA20190008), and AMED (24fm0208101j0008, 25fk0108694h0002) (to TN), Joint Research Project of the Institute of Medical Science, University of Tokyo; the Takeda Science Foundation (to YS and TN); and Joint Usage/Research Center Program of the Institute for Life and Medical Sciences at Kyoto University(to YS, YH, TN, and MH), the Takeda Science Foundation (to YS and TN).

The cryo-EM experiments were partially supported by the Platform Project for Supporting Drug Discovery and Life Science Research (Basis for Supporting Innovative Drug Discovery and Life Science Research (BINDS)) from AMED under Grant Number JP21am0101072 (support no. 3130) and JP23ama121001 (support no. 5890).

1022 **Author contributions**

1023 YS, YH, and MH conceptualized and designed the study and supervised all aspects of the
1024 research. YH and MH carried out gene cloning and protein expression. YS, YH, and SHG
1025 prepared specimens. YS conducted EM data collections, and YS and SHG analyzed cryo-EM
1026 data. YH performed fluorescent microscopy experiments, and MH performed the
1027 minireplicon assay. KT and TN provided essential resources and valuable advice throughout
1028 the study. YS and MH drafted the manuscript, which was further refined with input from all
1029 authors. All authors critically reviewed, edited, and approved the final version of the
1030 manuscript.

1031 **Declarations**

1032 The authors declare no competing interests.

1033 References

1034 1. Kuhn JH, Adkins S, Alkhovsky SV, et al (2022) 2022 taxonomic update of phylum
1035 Negarnaviricota (Riboviria: Orthornavirae), including the large orders Bunyavirales and
1036 Mononegavirales. Arch Virol 167:2857–2906. https://doi.org/10.1007/s00705-022-
1037 05546-z

1038 2. Lahaye X, Vidy A, Pomier C, et al (2009) Functional characterization of Negri bodies
1039 (NBs) in rabies virus-infected cells: Evidence that NBs are sites of viral transcription
1040 and replication. J Virol 83:7948–7958. https://doi.org/10.1128/JVI.00554-09

1041 3. Hoenen T, Shabman RS, Groseth A, et al (2012) Inclusion bodies are a site of ebolavirus
1042 replication. J Virol 86:11779–11788. https://doi.org/10.1128/JVI.01525-12

1043 4. Cifuentes-Muñoz N, Branttie J, Slaughter KB, Dutch RE (2017) Human
1044 Metapneumovirus Induces Formation of Inclusion Bodies for Efficient Genome
1045 Replication and Transcription. J Virol 91:e01282-17. https://doi.org/10.1128/JVI.01282-
1046 17

1047 5. Rincheval V, Lelek M, Gault E, et al (2017) Functional organization of cytoplasmic
1048 inclusion bodies in cells infected by respiratory syncytial virus. Nat Commun 8:563.
1049 https://doi.org/10.1038/s41467-017-00655-9

1050 6. Rudolph MG, Kraus I, Dickmanns A, et al (2003) Crystal structure of the borna disease
1051 virus nucleoprotein. Struct Lond Engl 1993 11:1219–1226

1052 7. Green TJ, Zhang X, Wertz GW, Luo M (2006) Structure of the vesicular stomatitis virus
1053 nucleoprotein-RNA complex. Science 313:357–360.
1054 https://doi.org/10.1126/science.1126953

1055 8. Albertini AAV, Wernimont AK, Muziol T, et al (2006) Crystal structure of the rabies
1056 virus nucleoprotein-RNA complex. Science 313:360–363.
1057 https://doi.org/10.1126/science.1125280

1058 9. Green TJ, Luo M (2009) Structure of the vesicular stomatitis virus nucleocapsid in
1059 complex with the nucleocapsid-binding domain of the small polymerase cofactor, P.
1060 Proc Natl Acad Sci 106:11713–11718. https://doi.org/10.1073/pnas.0903228106

1061 10. Tawar RG, Duquerroy S, Vonrhein C, et al (2009) Crystal structure of a nucleocapsid-
1062 like nucleoprotein-RNA complex of respiratory syncytial virus. Science 326:1279–
1063 1283. https://doi.org/10.1126/science.1177634

1064 11. Gutsche I, Desfosses A, Effantin G, et al (2015) Near-atomic cryo-EM structure of the
1065 helical measles virus nucleocapsid. Science 348:704–707.
1066 https://doi.org/10.1126/science.aaa5137

1067 12. Guryanov SG, Liljeroos L, Kasaragod P, et al (2015) Crystal Structure of the Measles
1068 Virus Nucleoprotein Core in Complex with an N-Terminal Region of Phosphoprotein. J
1069 Virol 90:2849–2857. https://doi.org/10.1128/JVI.02865-15

1070 13. Kirchdoerfer RN, Abelson DM, Li S, et al (2015) Assembly of the Ebola Virus
1071 Nucleoprotein from a Chaperoned VP35 Complex. Cell Rep 12:140–149.
1072 https://doi.org/10.1016/j.celrep.2015.06.003

1073 14. Leung DW, Borek D, Luthra P, et al (2015) An Intrinsically Disordered Peptide from
1074 Ebola Virus VP35 Controls Viral RNA Synthesis by Modulating Nucleoprotein-RNA
1075 Interactions. Cell Rep 11:376–389. https://doi.org/10.1016/j.celrep.2015.03.034

1076 15. Renner M, Bertinelli M, Leyrat C, et al (2016) Nucleocapsid assembly in pneumoviruses
1077 is regulated by conformational switching of the N protein. eLife 5:e12627.
1078 https://doi.org/10.7554/eLife.12627

1079 16. Sugita Y, Matsunami H, Kawaoka Y, et al (2018) Cryo-EM structure of the Ebola virus
1080 nucleoprotein-RNA complex at 3.6 Å resolution. Nature 563:137–140.
1081 https://doi.org/10.1038/s41586-018-0630-0

1082 17. Gérard FCA, Bourhis J-M, Mas C, et al (2022) Structure and Dynamics of the
1083 Unassembled Nucleoprotein of Rabies Virus in Complex with Its Phosphoprotein
1084 Chaperone Module. Viruses 14:2813. https://doi.org/10.3390/v14122813

1085 18. Kirchdoerfer RN, Saphire EO, Ward AB (2019) Cryo-EM structure of the Ebola virus
1086 nucleoprotein–RNA complex. Acta Crystallogr Sect F Struct Biol Commun 75:340–
1087 347. https://doi.org/10.1107/S2053230X19004424

1088 19. Zinzula L, Beck F, Klumpe S, et al (2021) Cryo-EM structure of the cetacean
1089 morbillivirus nucleoprotein-RNA complex. J Struct Biol 213:107750.
1090 https://doi.org/10.1016/j.jsb.2021.107750

1091 20. Fujita-Fujiharu Y, Sugita Y, Takamatsu Y, et al (2022) Structural insight into Marburg
1092 virus nucleoprotein–RNA complex formation. Nat Commun 13:1191.
1093 https://doi.org/10.1038/s41467-022-28802-x

1094 21. Hu S, Fujita-Fujiharu Y, Sugita Y, et al (2023) Cryoelectron microscopic structure of the
1095 nucleoprotein–RNA complex of the European filovirus, Lloviu virus. PNAS Nexus
1096 2:pgad120. https://doi.org/10.1093/pnasnexus/pgad120

1097 22. Zinzula L, Beck F, Camasta M, et al (2024) Cryo-EM structure of single-layered
1098 nucleoprotein-RNA complex from Marburg virus. Nat Commun 15:10307.
1099 https://doi.org/10.1038/s41467-024-54431-7

1100 23. Song X, Shan H, Zhu Y, et al (2019) Self-capping of nucleoprotein filaments protects the
1101 Newcastle disease virus genome. eLife 8:e45057. https://doi.org/10.7554/eLife.45057

1102 24. Ker D-S, Jenkins HT, Greive SJ, Antson AA (2020) CryoEM structure of the Nipah virus
1103 nucleocapsid assembly. Biophysics

1104 25. Gonnin L, Desfosses A, Bacia-Verloop M, et al (2023) Structural landscape of the
1105 respiratory syncytial virus nucleocapsids. Nat Commun 14:5732.
1106 https://doi.org/10.1038/s41467-023-41439-8

1107 26. Niller HH, Angstwurm K, Rubbenstroth D, et al (2020) Zoonotic spillover infections with
1108 Borna disease virus 1 leading to fatal human encephalitis, 1999–2019: an
1109 epidemiological investigation. Lancet Infect Dis 20:467–477.
1110 https://doi.org/10.1016/S1473-3099(19)30546-8

1111 27. Matsumoto Y, Hayashi Y, Omori H, et al (2012) Bornavirus Closely Associates and
1112 Segregates with Host Chromosomes to Ensure Persistent Intranuclear Infection. Cell
1113 Host Microbe 11:492–503. https://doi.org/10.1016/j.chom.2012.04.009

1114 28. Hock M, Kraus I, Schoehn G, et al (2010) RNA induced polymerization of the Borna
1115 disease virus nucleoprotein. Virology 397:64–72.
1116 https://doi.org/10.1016/j.virol.2009.11.016

1117 29. Sugita Y, Kawaoka Y, Noda T, Wolf M (2016) Structure of the Ebola Virus
1118 Nucleocapsid Core by Single Particle Cryo-Electron Microscopy. Microsc Microanal
1119 22:66–67. https://doi.org/10.1017/S1431927616001185

1120 30. Alayyoubi M, Leser GP, Kors CA, Lamb RA (2015) Structure of the paramyxovirus
1121 parainfluenza virus 5 nucleoprotein–RNA complex. Proc Natl Acad Sci U S A
1122 112:E1792–E1799. https://doi.org/10.1073/pnas.1503941112

1123 31. Shan H, Su X, Li T, et al (2021) Structural plasticity of mumps virus nucleocapsids with
1124 cryo-EM structures. Commun Biol 4:833. https://doi.org/10.1038/s42003-021-02362-0

1125 32. García J, García-Barreno B, Vivo A, Melero JA (1993) Cytoplasmic Inclusions of
1126 Respiratory Syncytial Virus-Infected Cells: Formation of Inclusion Bodies in
1127 Transfected Cells That Coexpress the Nucleoprotein, the Phosphoprotein, and the 22K
1128 Protein. Virology 195:243–247. https://doi.org/10.1006/viro.1993.1366

1129 33. Chenik M, Chebli K, Gaudin Y, Blondel D (1994) In Vivo Interaction of Rabies Virus
1130 Phosphoprotein (P) and Nucleoprotein (N): Existence of Two N-binding Sites on P
1131 Protein. J Gen Virol 75:2889–2896. https://doi.org/10.1099/0022-1317-75-11-2889

1132 34. Derdowski A, Peters TR, Glover N, et al (2008) Human metapneumovirus nucleoprotein
1133 and phosphoprotein interact and provide the minimal requirements for inclusion body
1134 formation. J Gen Virol 89:2698–2708. https://doi.org/10.1099/vir.0.2008/004051-0

1135 35. Zhang S, Chen L, Zhang G, et al (2013) An amino acid of human parainfluenza virus
1136 type 3 nucleoprotein is critical for template function and cytoplasmic inclusion body
1137 formation. J Virol 87:12457–12470. https://doi.org/10.1128/JVI.01565-13

1138 36. Zhou Y, Su JM, Samuel CE, Ma D (2019) Measles Virus Forms Inclusion Bodies with
1139 Properties of Liquid Organelles. J Virol 93:e00948-19.
1140 https://doi.org/10.1128/JVI.00948-19

1141 37. Hirai Y, Tomonaga K, Horie M (2021) Borna disease virus phosphoprotein triggers the
1142 organization of viral inclusion bodies by liquid-liquid phase separation. Int J Biol
1143 Macromol 192:55–63. https://doi.org/10.1016/j.ijbiomac.2021.09.153

1144 38. Ge P, Tsao J, Schein S, et al (2010) Cryo-EM Model of the Bullet-Shaped Vesicular
1145 Stomatitis Virus. Science 327:689–693. https://doi.org/10.1126/science.1181766

1146 39. Zhou K, Si Z, Ge P, et al (2022) Atomic model of vesicular stomatitis virus and
1147 mechanism of assembly. Nat Commun 13:5980. https://doi.org/10.1038/s41467-022-
1148 33664-4

1149 40. Jenni S, Horwitz JA, Bloyet L-M, et al (2022) Visualizing molecular interactions that
1150 determine assembly of a bullet-shaped vesicular stomatitis virus particle. Nat Commun
1151 13:4802. https://doi.org/10.1038/s41467-022-32223-1

1152 41. Riedel C, Vasishtan D, Pražák V, et al (2019) Cryo EM structure of the rabies virus
1153 ribonucleoprotein complex. Sci Rep 9:9639. https://doi.org/10.1038/s41598-019-46126-
1154 7

1155 42. Conley MJ, Short JM, Burns AM, et al (2022) Helical ordering of envelope-associated
1156 proteins and glycoproteins in respiratory syncytial virus. EMBO J 41:e109728.
1157 https://doi.org/10.15252/embj.2021109728

1158 43. Noda T, Kolesnikova L, Kolesnikova L, et al (2011) The Importance of the NP: VP35
1159 Ratio in Ebola Virus Nucleocapsid Formation. J Infect Dis 204:S878–S883.
1160 https://doi.org/10.1093/infdis/jir310

1161 44. Iseni F, Ruigrok RW, Blondel D, et al (1998) Characterization of rabies virus
1162 nucleocapsids and recombinant nucleocapsid-like structures. J Gen Virol 79:2909–2919.
1163 https://doi.org/10.1099/0022-1317-79-12-2909

1164 45. Esneau C, Raynal B, Roblin P, et al (2019) Biochemical characterization of the
1165 respiratory syncytial virus N0-P complex in solution. J Biol Chem 294:3647–3660.
1166 https://doi.org/10.1074/jbc.RA118.006453

1167 46. Liu B, Dong S, Li G, et al (2017) Structural Insight into Nucleoprotein Conformation
1168 Change Chaperoned by VP35 Peptide in Marburg Virus. J Virol 91:e00825-17.
1169 https://doi.org/10.1128/JVI.00825-17

1170 47. Croll TI (2018) *ISOLDE* : a physically realistic environment for model building into low-
1171 resolution electron-density maps. Acta Crystallogr Sect Struct Biol 74:519–530.
1172 https://doi.org/10.1107/S2059798318002425

1173 48. Aggarwal M, Leser GP, Kors CA, Lamb RA (2018) Structure of the Paramyxovirus
1174 Parainfluenza Virus 5 Nucleoprotein in Complex with an Amino-Terminal Peptide of
1175 the Phosphoprotein. J Virol 92:e01304-17. https://doi.org/10.1128/JVI.01304-17

1176 49. Yabukarski F, Lawrence P, Tarbouriech N, et al (2014) Structure of Nipah virus
1177 unassembled nucleoprotein in complex with its viral chaperone. Nat Struct Mol Biol
1178 21:754–759. https://doi.org/10.1038/nsmb.2868

1179 50. Leyrat C, Yabukarski F, Tarbouriech N, et al (2011) Structure of the vesicular stomatitis
1180 virus N^0-P complex. PLoS Pathog 7:e1002248.
1181 https://doi.org/10.1371/journal.ppat.1002248

1182 51. Brasseur R (1991) Differentiation of lipid-associating helices by use of three-dimensional
1183 molecular hydrophobicity potential calculations. J Biol Chem 266:16120–16127

1184 52. Mastronarde DN (2005) Automated electron microscope tomography using robust
1185 prediction of specimen movements. J Struct Biol 152:36–51.
1186 https://doi.org/10.1016/j.jsb.2005.07.007

1187 53. Zivanov J, Nakane T, Forsberg BO, et al (2018) New tools for automated high-resolution
1188 cryo-EM structure determination in RELION-3. eLife 7:e42166.
1189 https://doi.org/10.7554/eLife.42166

1190 54. Punjani A, Rubinstein JL, Fleet DJ, Brubaker MA (2017) cryoSPARC: algorithms for
1191 rapid unsupervised cryo-EM structure determination. Nat Methods 14:290–296.
1192 https://doi.org/10.1038/nmeth.4169

1193 55. Punjani A, Zhang H, Fleet DJ (2020) Non-uniform refinement: adaptive regularization
1194 improves single-particle cryo-EM reconstruction. Nat Methods 17:1214–1221.
1195 https://doi.org/10.1038/s41592-020-00990-8

1196 56. Bepler T, Morin A, Rapp M, et al (2019) Positive-unlabeled convolutional neural
1197 networks for particle picking in cryo-electron micrographs. Nat Methods 16:1153–1160.
1198 https://doi.org/10.1038/s41592-019-0575-8

1199 57. Goddard TD, Huang CC, Meng EC, et al (2018) UCSF ChimeraX: Meeting modern
1200 challenges in visualization and analysis. Protein Sci 27:14–25.
1201 https://doi.org/10.1002/pro.3235

1202 58. Emsley P, Lohkamp B, Scott WG, Cowtan K (2010) Features and development of Coot.
1203 Acta Crystallogr D Biol Crystallogr 66:486–501.
1204 https://doi.org/10.1107/S0907444910007493

1205 59. Murshudov GN, Skubák P, Lebedev AA, et al (2011) *REFMAC* 5 for the refinement of
1206 macromolecular crystal structures. Acta Crystallogr D Biol Crystallogr 67:355–367.
1207 https://doi.org/10.1107/S0907444911001314

1208 60. Yamashita K, Palmer CM, Burnley T, Murshudov GN (2021) Cryo-EM single-particle
1209 structure refinement and map calculation using *Servalcat*. Acta Crystallogr Sect Struct
1210 Biol 77:1282–1291. https://doi.org/10.1107/S2059798321009475

1211 61. Nicholls RA, Fischer M, McNicholas S, Murshudov GN (2014) Conformation-
1212 independent structural comparison of macromolecules with *ProSMART*. Acta
1213 Crystallogr D Biol Crystallogr 70:2487–2499.
1214 https://doi.org/10.1107/S1399004714016241

1215 62. Brown A, Long F, Nicholls RA, et al (2015) Tools for macromolecular model building
1216 and refinement into electron cryo-microscopy reconstructions. Acta Crystallogr D Biol
1217 Crystallogr 71:136–153. https://doi.org/10.1107/S1399004714021683

1218 63. Reuter A, Horie M, Höper D, et al (2016) Synergistic antiviral activity of ribavirin and
1219 interferon-α against parrot bornaviruses in avian cells. J Gen Virol 97:2096–2103.
1220 https://doi.org/10.1099/jgv.0.000555

1221 64. Thomas Williams, Colin Kelley, and many others (2024) Gnuplot: An Interactive Plotting
1222 Program

1223 65. Katoh K, Standley DM (2013) MAFFT Multiple Sequence Alignment Software Version
1224 7: Improvements in Performance and Usability. Mol Biol Evol 30:772–780.
1225 https://doi.org/10.1093/molbev/mst010

1226 66. Robert X, Gouet P (2014) Deciphering key features in protein structures with the new
1227 ENDscript server. Nucleic Acids Res 42:W320–W324.
1228 https://doi.org/10.1093/nar/gku316

1229

Fig. 1

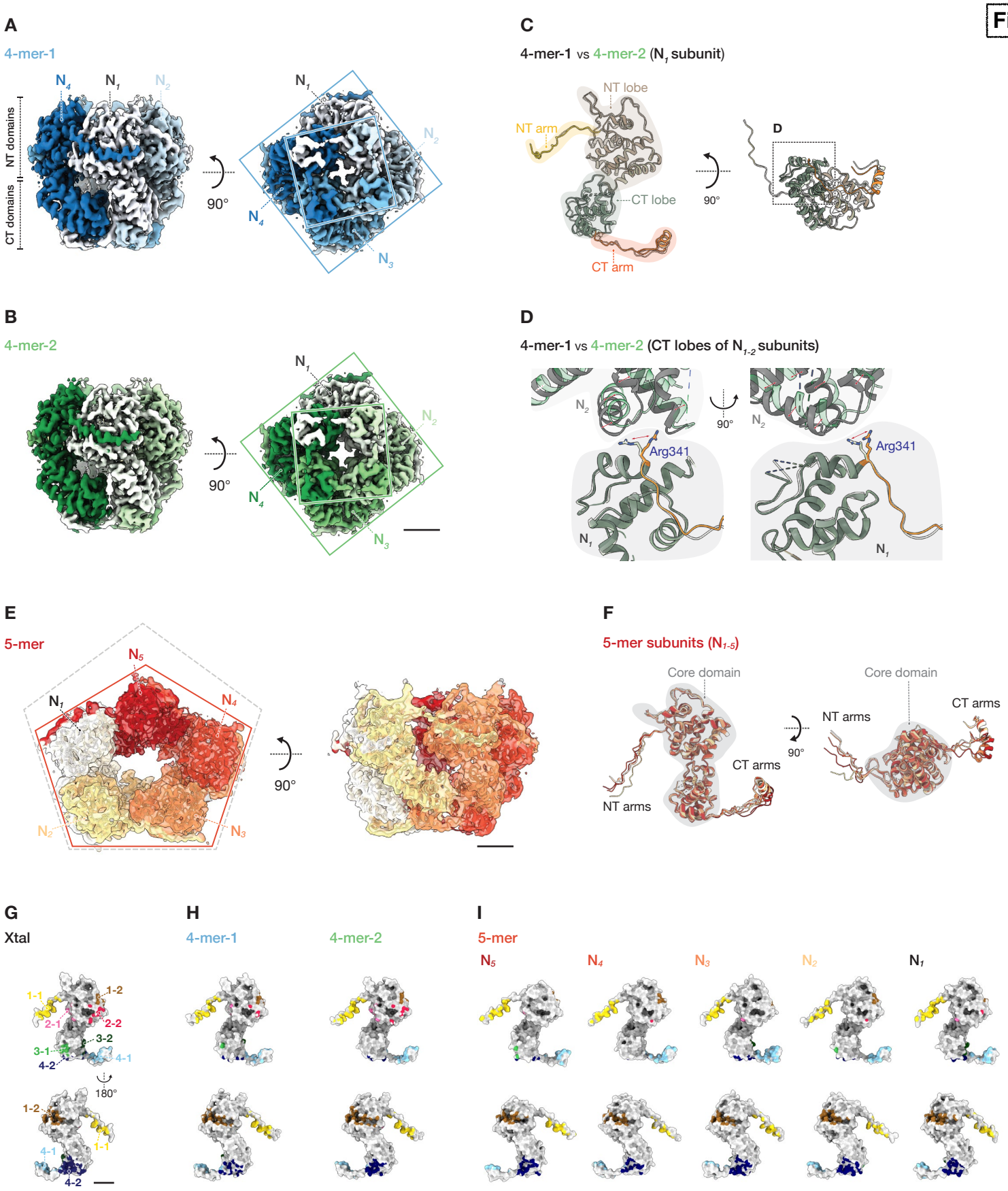
A
4-mer-1
NT domains
CT domains
N4
N1
N2
N3
90°
B
4-mer-2
C
4-mer-1 vs 4-mer-2 (N1 subunit)
NT lobe
NT arm
CT lobe
CT arm
D
4-mer-1 vs 4-mer-2 (CT lobes of N1-2 subunits)
Arg341
E
5-mer
N5
F
5-mer subunits (N1-5)
Core domain
NT arms
CT arms
G
Xtal
1-1
1-2
2-1
2-2
3-1
3-2
4-1
4-2
180°
H
4-mer-1
4-mer-2
I
5-mer

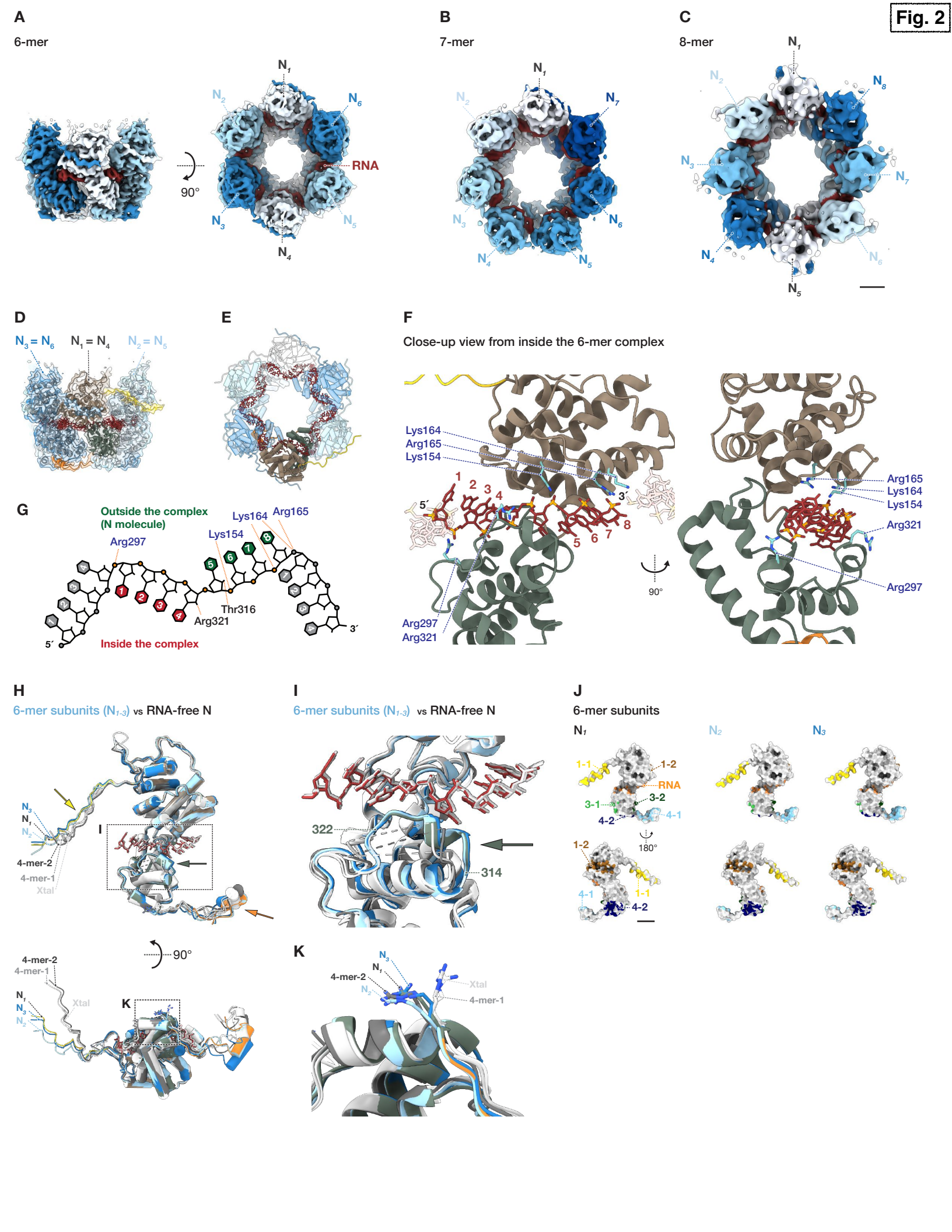
Fig. 2
A
6-mer
N1
N2
N6
RNA
90°
N3
N5
N4
B
7-mer
N1
N2
N7
N3
N6
N4
N5
C
8-mer
N1
N2
N8
N3
N7
N4
N6
N5
D
N3 = N6
N1 = N4
N2 = N5
E
F
Close-up view from inside the 6-mer complex
Lys164
Arg165
Lys154
1
2
3
4
5
6
7
8
5´
3´
90°
Arg297
Arg321
Arg165
Lys164
Lys154
Arg321
Arg297
G
Outside the complex
(N molecule)
Arg297
Lys154
Lys164
Arg165
Thr316
Arg321
5´
3´
Inside the complex
H
6-mer subunits (N1-3) vs RNA-free N
N3
N1
N2
I
4-mer-2
4-mer-1
Xtal
90°
4-mer-2
4-mer-1
N1
N3
N2
Xtal
K
I
6-mer subunits (N1-3) vs RNA-free N
322
314
K
N3
N1
4-mer-2
N2
Xtal
4-mer-1
J
6-mer subunits
N1
N2
N3
1-1
1-2
RNA
3-1
3-2
4-2
4-1
180°
1-2
4-1
1-1
4-2

Fig. 3

A

Flat 6-mer

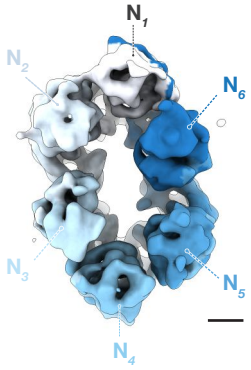

D

Flat 6-mer subunits

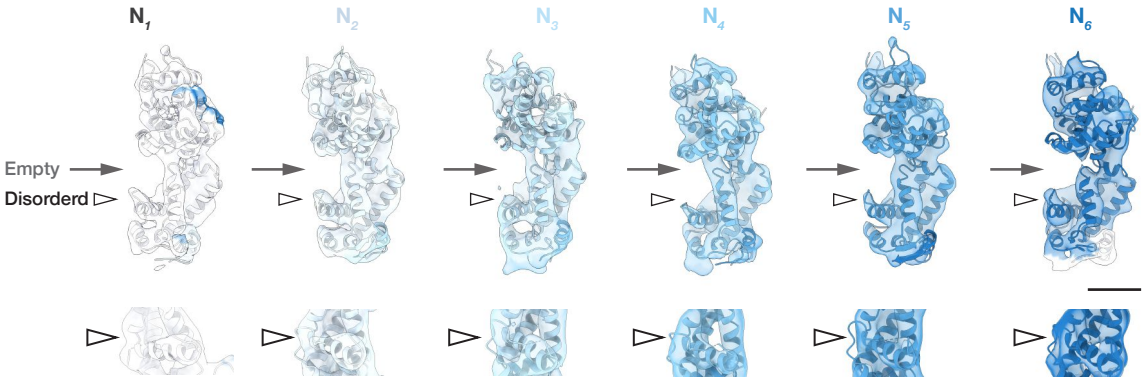

B

Oval 6-mer-1

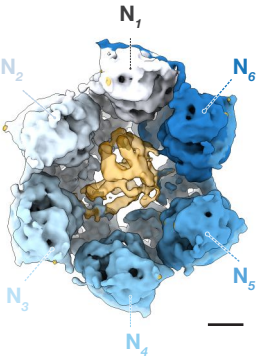

E

Oval 6-mer-1 subunits

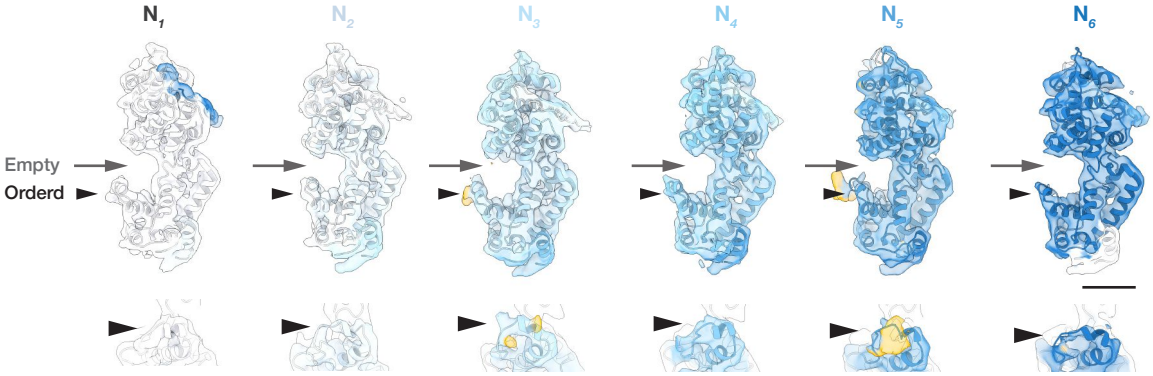

C

Oval 6-mer-2

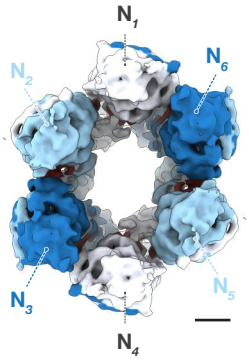

F

Oval 6-mer-2 subunits

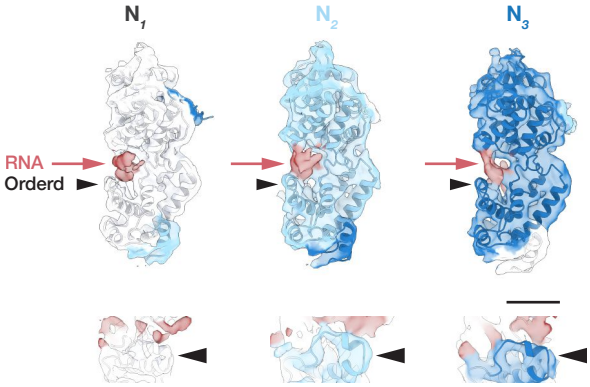

G

6-mer subunits

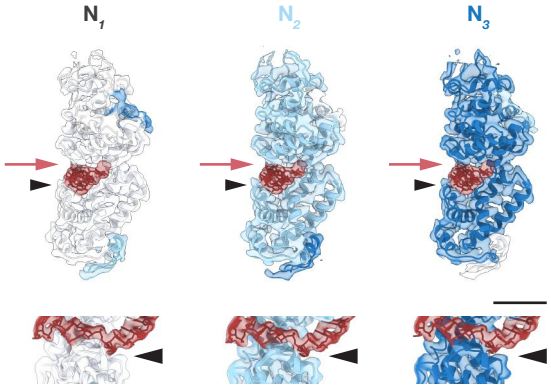

Fig. 4

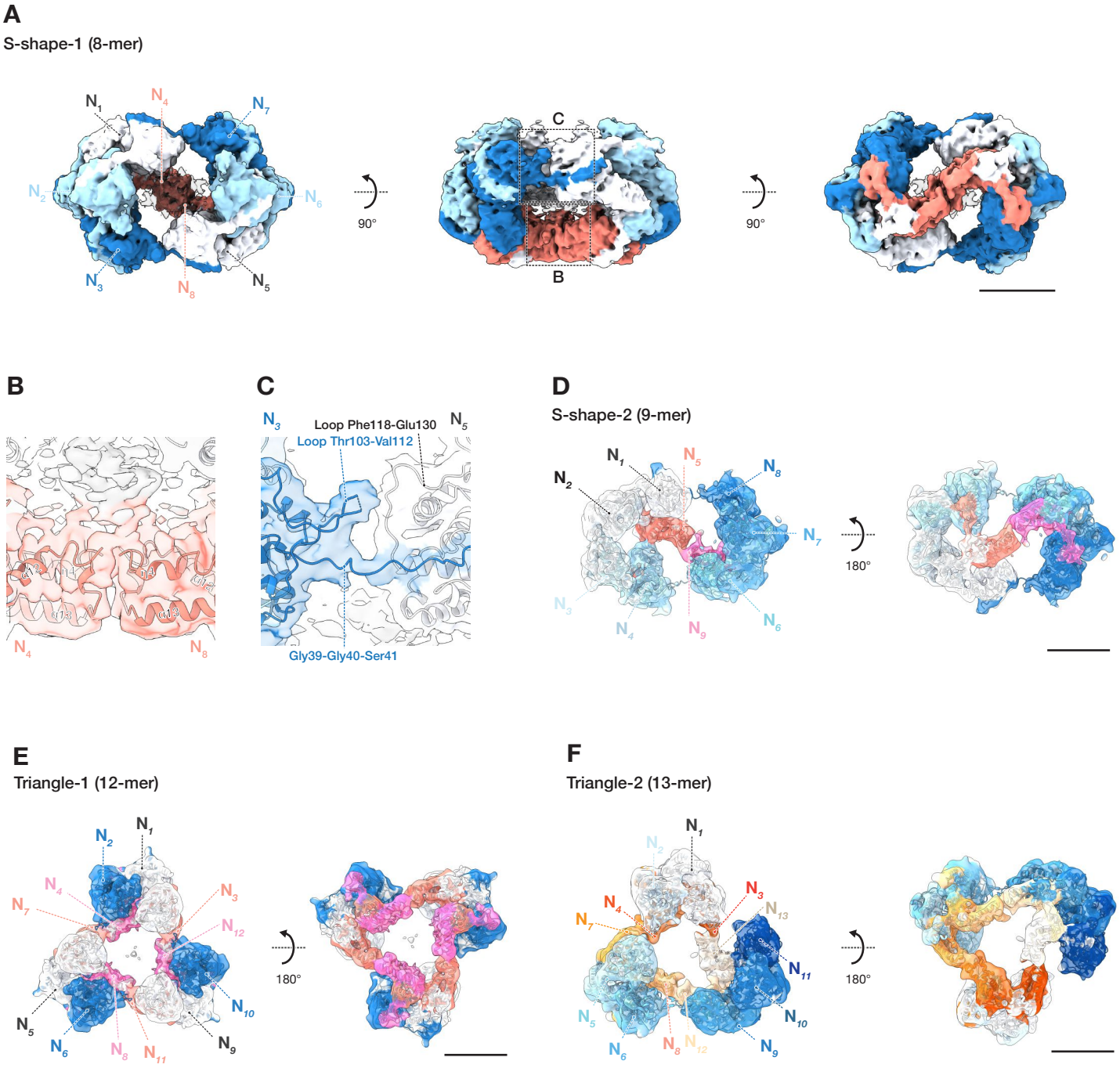
A
S-shape-1 (8-mer)
N1
N4
N7
N2
N6
N3
N8
N5
90°
C
B
90°
B
C
N3
Loop Phe118-Glu130
N5
Loop Thr103-Val112
Gly39-Gly40-Ser41
N4
N8
D
S-shape-2 (9-mer)
N1
N5
N8
N2
N7
180°
N3
N4
N9
N6
E
Triangle-1 (12-mer)
N1
N2
N4
N3
N7
N12
180°
N10
N5
N6
N8
N11
N9
F
Triangle-2 (13-mer)
N1
N2
N3
N4
N13
N7
N11
180°
N10
N5
N6
N8
N12
N9

Fig. 5

A

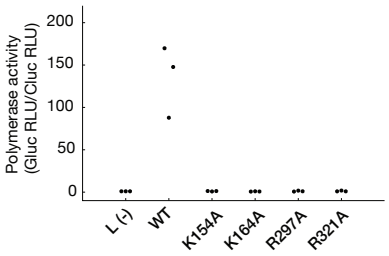

B

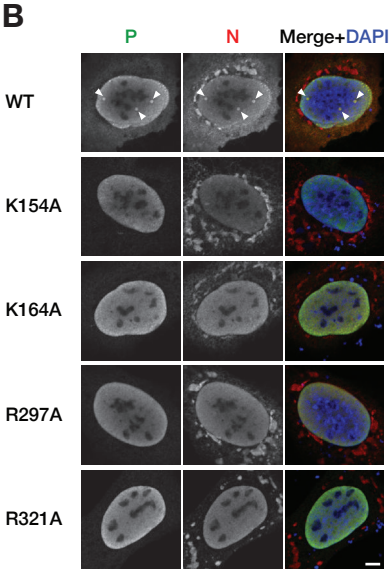

C

4-mer: N(K164A)

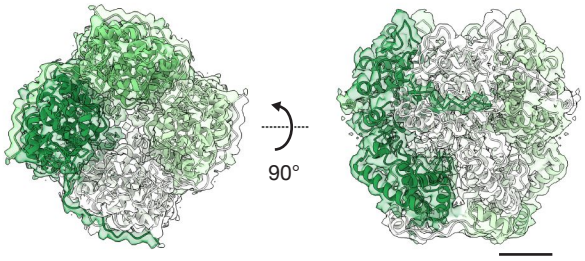

D

4-mer: N(K164A) vs WT (4-mer-2)

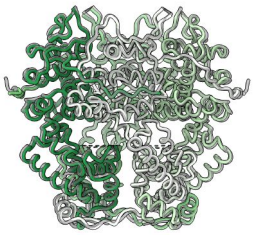

E

5-mer: N(K164A) vs WT

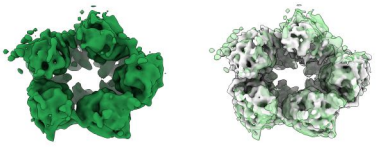

F

S-shape: N(K164A) vs WT (S-shape-1)

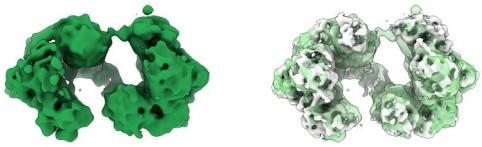

G

Flat 6-mer: N(K164A) vs WT

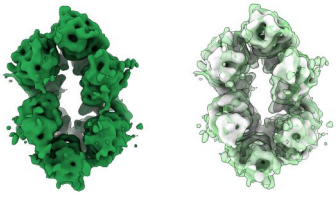

H

4-mer antiparallele: N(K164A) vs WT

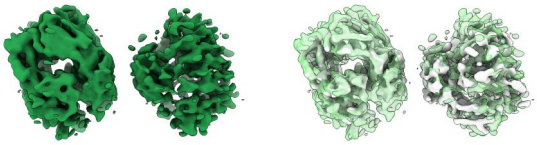

I

6-mer: WT

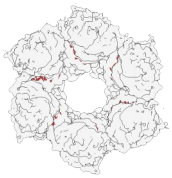

J

6-mer: N(K164A) vs WT

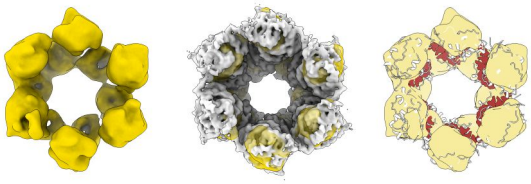

K

7-mer: N(K164A) vs WT

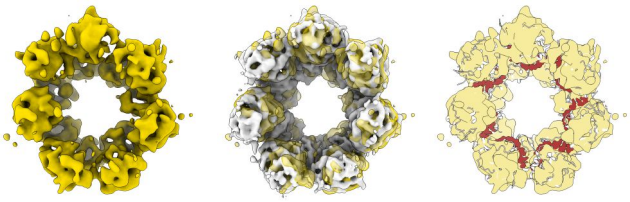

L

Oval 6-mer: N(K164A) vs WT (oval 6-mer-2)

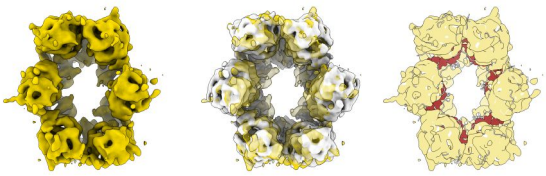

M

Flat 7-mer: N(K164A)

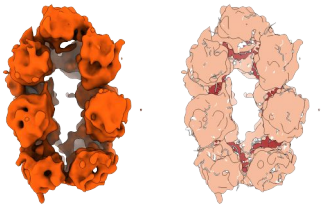

N

Triangular 6-mer: N(K164A)

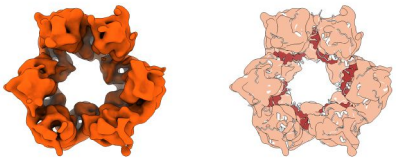

Fig. 6

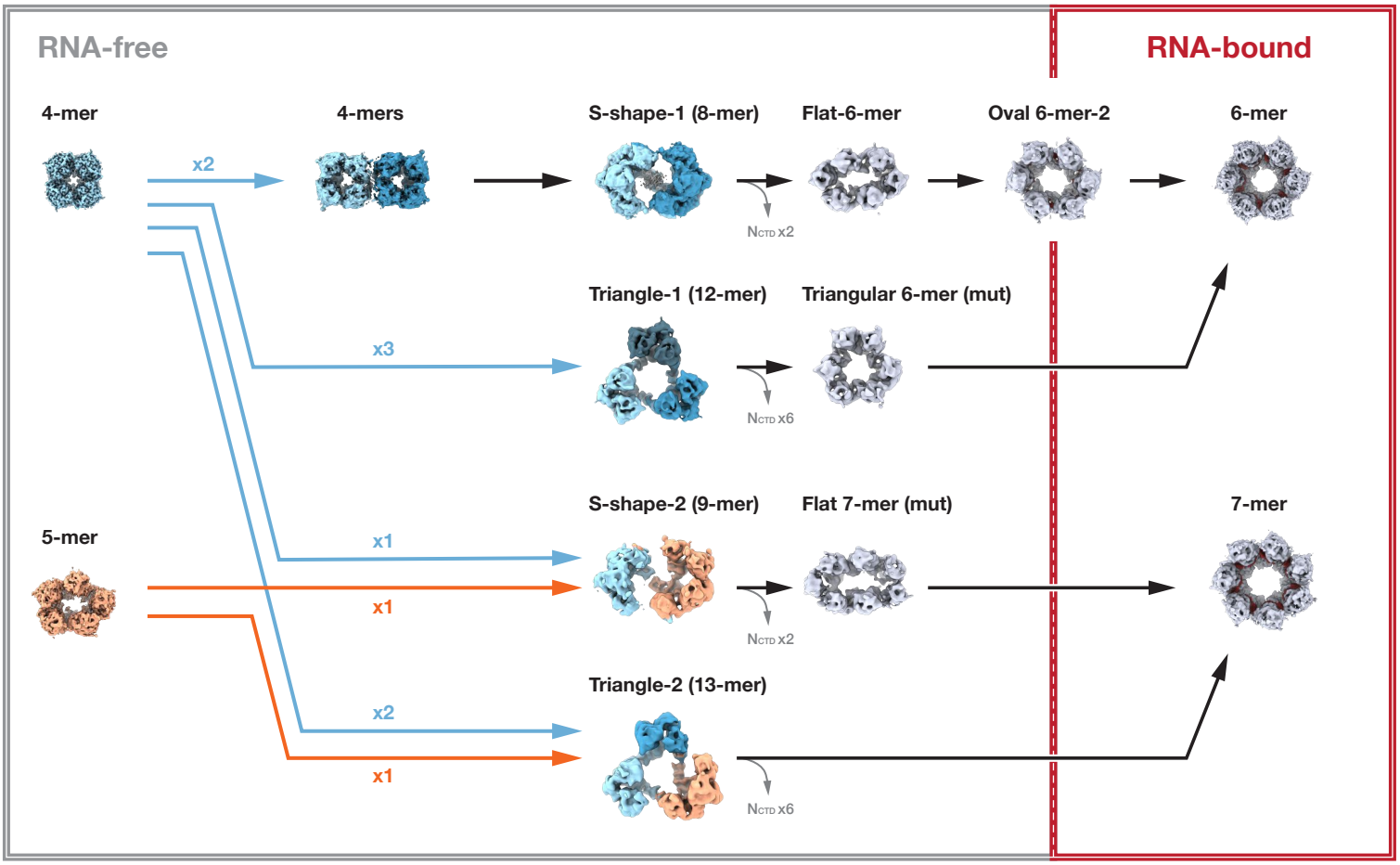
RNA-free
RNA-bound
4-mer
4-mers
S-shape-1 (8-mer)
Flat-6-mer
Oval 6-mer-2
6-mer
x2
NCTD x2
Triangle-1 (12-mer)
Triangular 6-mer (mut)
x3
NCTD x6
S-shape-2 (9-mer)
Flat 7-mer (mut)
7-mer
5-mer
x1
x1
NCTD x2
Triangle-2 (13-mer)
x2
x1
NCTD x6